ResearchGate

See discussions, stats, and author profiles for this publication at: https://www.researchgate.net/publication/327671682

Aerothermodynamic effects of controlled heat release within the hypersonic shock layer around a large angle blunt cone

Article *in* Physics of Fluids · September 2018

DOI: 10.1063/1.5046191

CITATIONS
8

READS
376

2 authors:

Sneh Deep
Indian Institute of Science
17 PUBLICATIONS **140** CITATIONS

SEE PROFILE

Jagadeesh Gopalan
Indian Institute of Science
297 PUBLICATIONS **2,376** CITATIONS

SEE PROFILE

Some of the authors of this publication are also working on these related projects:

Project Hypersonic Aerodynamics View project

Project Laser induced fluorescence View project

All content following this page was uploaded by Sneh Deep on 06 October 2018.

The user has requested enhancement of the downloaded file.

AIP Publishing

This manuscript was accepted by Phys. Fluids. Click here to see the version of record.

Aerothermodynamic effects of controlled heat release within the hypersonic shock layer around a large angle blunt cone

Sneh Deep,[a] G. Jagadeesh
Department of Aerospace Engineering, Indian Institute of Science, Bangalore-560012, India

Effects of controlled heat addition into the high temperature, chemically reacting shock layer of a large angle (60 deg.) blunt cone with a spherical nose have been experimentally investigated. The exothermic oxidation of ablated chromium from the surface of the cone at hypersonic Mach numbers triggers the heat release process. A conical skirt with a base diameter of 70 mm and a semi-apex angle of 30º, culminating into a nose of radius 30 mm has been used as the test model. An in-house hypersonic free-piston driven shock tunnel facility, HST3, was used for the experiments at a stagnation enthalpy of 6.31 MJ/kg and a freestream Mach number of 9.84. The temperature distribution in the shock layer was experimentally measured by the Two-Color Ratio Pyrometry (TCRP) technique, using a Digital Single Lens Reflex (DSLR) camera as a pyrometer. The temperature field was corrected for discrete radiative line emissions obtained through emission spectroscopy. Surface heat flux measurements were done using carefully calibrated thin film platinum heat transfer gauges mounted on an insulating Macor substrate. Shock stand-off distances were measured through Schlieren imaging of the flow using a high-speed camera at 20,000 frames per second, and also by a new intensity-scan based method using the processed color image from the DSLR camera. Calculations showed a 173 K rise in the temperature of the gas layer in the stagnation region due to chromium oxidation. The net surface heat flux on the blunt cone was also found to increase by about 31 W/cm^2. The shock stand-off distance, as ascertained from Schlieren images, increased from about 3.82 mm (± 1.4%) to 4.45 mm (± 1.5%), a 17% rise. Analytical calculations, taking chromium oxidation reaction kinetics into consideration- to relate the total exothermic heat release to its distribution into various processes demonstrated that chromium oxidation releases about 78 W/cm^2 energy in the stagnation region of the shock layer. 1.9% of this energy increases the temperature of the gas layer, 40% is convected back into the airframe, 0.4% is lost from the rear of the Macor substrate by conduction and about 8% is radiated into the model. Remaining 50% of the heat was used up in pushing the shock layer away from the body by raising its density, thereby increasing shock stand-off distance.

ACCEPTED MANUSCRIPT

I. INTRODUCTION

Hypersonic flow is a regime where certain flow phenomena become markedly important and render such flows physically different from supersonic flows.[1] The region between a shock wave and a blunt body, called a shock layer, is very thin in case of hypersonic flows. One of the earliest attempts to experimentally determine the shock layer thickness (alternatively the shock stand-off distance) led to a simple yet important observation that the dimensionless shock layer thickness is typically proportional to the inverse density ratio across the shock.[2] At high M_∞, density jump across the shock increases, resulting in a thin shock layer. Another important aspect of hypersonic flows is the presence of a relatively thick boundary layer (BL).[1,3] The inherent abundant kinetic energy present in high-velocity hypersonic flows is manifested as the internal energy of the gas within the BL-due to the viscous effects inside it. This increases the gas layer temperature, which in turn reduces its density. To maintain the mass flow rate through the boundary layer a constant, the BL thickness increases. For extremely high Mach numbers, the BL on a hypersonic vehicle may become very thick and merge with the thin shock wave, 'interacting' with it, making the entire shock layer fully viscous. Such effects influence the aerothermodynamics of hypersonic vehicles,[4] mainly drag, lift and aerodynamic heating of the vehicle surface.

Strong viscous interaction has a tendency of increasing the wall surface pressure over the value that would exist for a similar inviscid flow. Increased pressure manifests itself in the form of increased drag. Simultaneously, the extreme temperatures in the shock layer- sometimes as high as 12,000 K for typical re-entry missions, may lead to massive aerodynamic heating of the vehicle airframe and its subsequent collapse if not addressed properly. It is for this reason that aerodynamic heating is considered the most dominant aspect governing the design of all hypersonic equipment. Several ideas have been proposed till date to alter the viscous shock layer and alleviate the adverse effects of high temperature hypersonic flows. With the classic discovery by Allen and Eggers, back in 1951 that blunt shapes serve as efficient heat shields it was recognized that relatively blunted bodies would be the future of space shuttle air-frame design, drastically reducing the maximum heat transfer rate by dissipating most of it in the air surrounding the body. However, blunt nosed vehicles present their own problem of large wave drag, which is desirable during the reentry phase of such

a) Electronic mail: snehdeep@iisc.ac.in

AIP Publishing

vehicles but proves to be a nightmare during the ascent phase, affecting the efficiency of the propulsion system. To address this problem, various drag reduction techniques have been employed. These include introduction of a sharp-tipped spike protruding from the stagnation point of the blunt model,[5,6] counter flow supersonic jet,[7] combination of an opposing supersonic jet and an aerospike,[8] energy deposition using an electric arc discharge,[9] and addition of a multi-step after body at the model base.[10] All these techniques, though extremely effective in diminishing wave drag, are rather difficult to implement in practical re-entry missions. Numerous studies, both experimental and computational, have also convincingly proved the efficacy of heat deposition as an alternate means of alleviating wave drag experienced by high speed aerospace vehicles, in addition to those referred. Experiments performed in the mid-1960s and early-1980s showed that burning hydrogen in a region of spike-induced separated flow caused significant drag reduction, over and above that achievable with an ordinary aerospike.[11,12] Intricate numerical studies of this configuration were later done to complement the experimental results.[13]

Kulkarni et al, on similar lines performed heat addition experiments by coating the surface of the model with chromium. Chromium oxidation was found to reduce drag by a significant amount by a mechanism explained later. Tahsini's[14] numerical investigation of the heat addition problem provided better insight into the chemical kinetics of the reactions involved at higher enthalpies. Simulations confirmed a reduction in drag, though not as much as that obtained from experiments. Although heat addition has a desirable effect of drag reduction, its effect on the surface heat flux due to a chemically reacting boundary layer must be carefully addressed before commenting on its affectivity in practical applications. Such studies, involving thermodynamic effects of controlled heat addition due to metal oxidation is absent in contemporary literature. Most of the research is confined to studying the effect of heat addition on drag on various geometries. Shneider[15] studied change in aerodynamic forces due to plasma heat addition in supersonic flow (Mach 3). Cai et al[16] performed analytical calculations and numerical simulations to study energy deposition effects on pressure forces in supersonic flow over a wedge. Marconi[17] modeled heat addition to reduce drag and sonic boom on a re-entry type vehicle flying at supersonic speed. Riggins et al[18] computed effect of energy deposition on wave drag over axisymmetric blunt bodies at hypersonic flow conditions.

In addition to drag forces, heat addition also affects the temperature distribution in the shock layer and the shock stand-off distance. Current literature is replete with various invasive[19-21] and non-invasive[22-24] temperature measurement techniques. Invasive techniques, as the name suggests, interfere with the subject of interest itself and disturb the temperature field. They are therefore limited in their applications. Most non-invasive techniques, although better than their invasive counterparts, employ infrared cameras (IR) or emission spectroscopy. They rely on the knowledge of the emissivity of the source, which is rarely a constant and sometimes difficult to determine for dissociating media. A particular solution to this is the Two-Color Ratio Pyrometry (TCRP),[25] a ratio based temperature measurement technique that is independent of the emissivity of the subject. In the recent past, TCRP using commercially available digital cameras[26-28] has gained significant prominence for spatially resolved temperature measurements.

Several empirical relations[29-31] and experimental data[32-34] exist for predicting the shock stand-off distance over spherical bodies or those with a blunt spherical nose subjected to hypersonic flow conditions. However, most of them are limited to ideal gases, rendering them inaccurate for predicting shock stand-off distance in real gas flows, marked by substantial dissociation.[35]

In this work, we explore the effects of controlled heat addition technique by coating the surface of a large angle blunt cone with a thin film of chromium. We study coating effects on the thermodynamics of the shock layer- by characterizing its consequence on temperature distribution in the shock layer, the net surface heat flux on the model and the shock stand-off distance. The technique involves heat release through exothermic oxidation of chromium in the presence of nascent oxygen formed in the dissociating gas layer. Heat addition augments the shock layer temperature and reduces the pressure and density behind the shock wave, causing drag reduction.[36] The greatest advantage of this technique is its relative simplicity. Being a passive technique, it utilizes the properties of the shock layer itself for chromium ablation and heat addition, without the need for carrying any working fluid as a coolant. Experiments performed for shock layer characterization due to heat release in a high enthalpy environment, as much as 6.3 MJ/kg, in the free-piston driven shock tunnel facility (FPST) are a first of their kind, to the best of our knowledge.

We begin by first characterizing the temperature distribution in the shock layer and reporting the difference caused due to chromium presence. The TCRP technique developed recently in the laboratory independently by us,[37] has been used for measuring the spatial distribution of temperature field in the shock layer as well as in the hypersonic flow field around the blunt cone.

We next report the percentage change (due to chromium coating) observed in the heat flux measured on the surface of a blunt cone model using platinum thin film heat transfer gauges. Heat flux data without chromium coating have been complemented with illustrative computations performed in ANSYS FLUENT 14.5, taking dissociation effects at high enthalpy into account. Comparison has also been made with the analytical heat flux expression over blunt cones due to Lester Lees.[38] The measured temperature is used to predict the stagnation point heat flux in dissociated air using the classic Fay and Riddell expression.[39]

ACCEPTED MANUSCRIPT

AIP Publishing

This manuscript was accepted by Phys. Fluids. Click here to see the version of record.

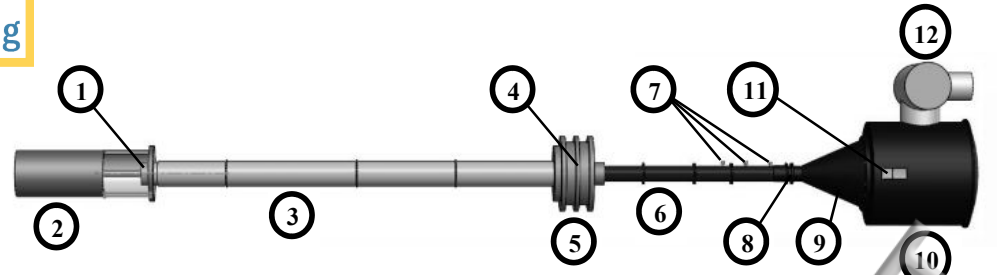

FIG. 1. Hypersonic shock tunnel 3.

1 Piston
2 Reservoir
3 Compression/ driver tube
4 Location of metal diaphragm
5 Inertial weight
6 Shock/ driven tube
7 Pressure transducers
8 Location of paper diaphragm
9 De Laval (C-D) nozzle
10 Dump tank
11 Optical window
12 High vacuum system

Next, the effect of chromium film on the shock stand-off distance has been studied and reported. We measure shock stand-off distances by standard Schlieren imaging technique using a high-speed camera and a new intensity-scan based technique using the processed image from the Digital Single Lens Reflex (DSLR) camera.

Finally, an analytic energy balance has been carried out to first ascertain the total energy deposited into the shock layer due to chromium regression and then interpret the distribution of the liberated energy into various processes.

II. EXPERIMENTAL FACILITY AND PROCEDURE

A. The Shock Tunnel

All the experiments were performed in the Hypersonic Shock Tunnel (HST) 3, also known as the Free Piston Driven Shock Tunnel (FPST), stationed in the Laboratory for Hypersonic and Shock Wave Research (LHSR) at the Indian Institute of Science. A schematic of HST3 is shown in Fig. 1. It essentially consists of a high-pressure reservoir attached to a stainless-steel compression tube (driver). The compression tube is followed by a shock tube (driven). The shock tube in turn is connected to a conical convergent-divergent nozzle which has a divergence angle of 10º and an exit diameter of 295 mm. A throat insert is used in the nozzle, providing a throat diameter of 12.5 mm. The nozzle opens into a dump tank. Test models are mounted in its test section. A 20 kg piston is initially at the confluence of the reservoir and the compression tube. Upon release, the piston moves down the tube, accelerating and gaining considerable kinetic energy from the expanding reservoir gas (nitrogen). This energy is manifested into compressing the driver gas, until the metal diaphragm separating the compression tube and shock tube ruptures, and shock tube flow ensues. Shock speed in the shock tube was measured using three pressure transducers mounted on the shock tube, separated by a known distance. Measurements indicated a shock attenuation of less than 1% over the instrumented portion of the shock tube. As the incident shock moves past the transducers, it is reflected by a paper diaphragm placed between the shock tube and the nozzle entrance, rupturing it and stagnating the gas behind it. The transducer closest to the paper diaphragm was used to measure the pressure in the stagnation region.

Vacuum conditions are initially maintained in the dump tank with the aid of a high vacuum system. Under such conditions, the flow is choked at the nozzle throat, and the test gas expands through it, entering the test section at hypersonic speeds. A pitot pressure transducer helps obtain the steady test time available from the flow. The test section is fitted with optical windows for various flow diagnostics. The HST3 is capable of simulating stagnation enthalpies of up to 25 MJ/kg. More design details of the HST3 and its working may be found in C. S. Kumar.[40]

B. Test model

The test model used had a conical skirt with a base diameter of 70 mm and a semi-apex angle of 30º, culminating into a nose of radius 30 mm. These sphere-cone sections, with a strategically placed center of mass, are known to provide excellent aerodynamic stability from entry to surface impact. The proposed experiments were first performed on an uncoated blunt cone model. After completion of a set of experiments, the entire surface of the model was coated with a uniform 10 µm thick film of 99% pure Chromium (henceforth referred to as Cr) by electrodeposition and the experiments were repeated. For reasons mentioned in Section III B, temperature measurements were also performed with Cr coated only in the region bounded by the intersection of the sonic curve with the model surface. The photograph of the model coated with Cr on its entire surface has been shown in Fig. 2(a), whereas Fig. 2(b) depicts the

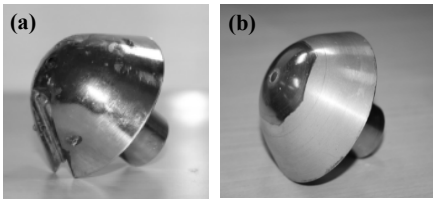

FIG. 2. Large angle blunt cone model for experiments. (a) Cr coated on entire surface; (b) Cr coated only in the sonic circle.

ACCEPTED MANUSCRIPT

AIP Publishing

model coated only within its sonic circle. The models were provided with a sting to mount them in the test section.

C. Heat flux measurements

For convective heat flux measurements into the model, platinum (Pt) thin film gauges were hand painted on an insulating MACOR substrate, which was then flush mounted into slots cut on the model surface. The specific location of the gauges on the model surface has been illustrated schematically in Fig. 3. The actual chromium coated model with gauges marked 1-5 has also been included as an inset. Gauge 1 indicates that at the stagnation point. Gauges mounted symmetrically on the other side of the stagnation point (2a-5a) have not been shown in the figure. Time dependent problem of thin film platinum gauges is one of conduction into a slab of material (Pt) mounted on a 'semi-infinite extent' of another material (Macor). Calculations[41] have shown that for our test time of 315 µsec and Macor thermal diffusivity of 7.94×10^{-7} m^2/s, a Macor thickness (depth) of 3 mm is sufficient for it to qualify as semi-infinite and for transient, 1-D conduction to occur within the solid if sudden heat flux be imposed at the exposed side. We have maintained a thickness of 5 mm of the substrate. Starting at the governing 1D transient heat conduction equation, the expression for unsteady, heat transfer rate at the surface of the Macor substrate, assuming negligible thickness of the Pt film (compared to that of the substrate), is as follows:

$$\dot{q}(t) = \frac{\beta}{\sqrt{\pi}\alpha E_0}\left(\frac{E(t)}{\sqrt{t}} + \frac{1}{2}\int_0^t \frac{E(t)-E(\tau)}{(t-\tau)^{1.5}}\,d\tau\right) \qquad (1)$$

where $\beta = \sqrt{\rho c k}$ is the thermal product of Macor, $\alpha = E/E_0 t$ is the temperature coefficient of the Pt film, and E_0 is the initial film voltage, measured just before performing the experiments. ρ, c and k are respectively the density, specific heat and thermal conductivity of the Macor substrate. $E(t)$ is the voltage variation across the gauge due a change in its resistance due to heat transfer from the shock layer. This quantity is directly measured from experiments. The voltage signal, which is a function of time, is approximated as a piecewise linear function and the integral term in Eq. (1) is evaluated using a standard numerical algorithm,[42] which yields an expression for heat flux. The average heat flux during the steady test time is then reported. All the gauges had an initial resistance of less than 50 Ω. Each had a length and width of about 8 mm and 1 mm respectively. α and β are determined via a pre-calibration[40] to be 0.000811 K^{-1} (±0.7%) and 1715 Wm^{-2}K^{-1}s$^{-1/2}$ (±4%) respectively.

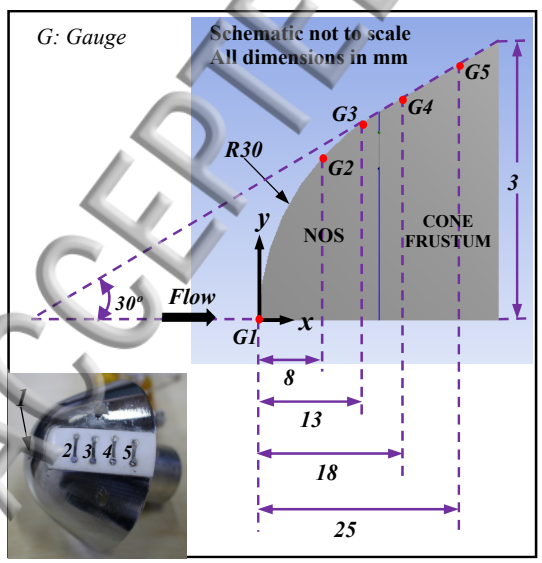

FIG. 3. Gauge locations on the model surface. Inset-Photograph of Cr coated model with gauges marked.

D. Temperature characterization of the shock layer

A Canon EOS 750D DSLR camera, with an EF-S lens kit of 18-55 mm focal length, was used for procuring 'raw' images in our experiments. It offers the necessary manual user control settings and a 14-bit raw data format in each of the R, G and B color channels. It is based on a CMOS sensor (22.3 mm×14.9 mm) with 24 million effective pixels. A spectrally calibrated light source, Thorlabs SLS201/M stabilized tungsten-halogen calibration lamp, and Newport's 77250-MC hand operated monochromator were used for the spectral calibration of the camera, relating the intensity in the color channels in arbitrary units to the actual spectral radiance of the source. It uses a model 77298 Grating Assembly, ruled with 1200 lines/ mm, 360 nm blaze and 200-1000 nm wavelength range. Before using the monochromator for camera calibration, the responsivity of the monochromator was characterized using the calibration lamp along with a Newport 818-BB-27 biased photodetector of known spectral response.

The Two-Color Ratio Pyrometry technique (TCRP), based on the Planck's Law of spectral intensity of electromagnetic radiation emitted by a real body, was employed to characterize the temperature distribution in the shock layer formed in front of the large-angle blunt cone.

$$L_\lambda(\lambda,T) = \varepsilon(\lambda,T)\,\frac{2hc^2}{\lambda^5}\,\frac{1}{exp(hc/\lambda kT)-1} \qquad (2)$$

where L=spectral radiance per unit wavelength, h=Planck constant, c=speed of light in the medium, k=Boltzmann constant, ε=surface emissivity of the body. The spectral radiance is a function of both the wavelength of interest and temperature of the subject.

The basic assumptions involved in applying the technique, the rationale behind the suitability of a commercial DSLR camera as a ratio pyrometer, and the detailed calibration of the color filter array (CFA) and the imaging system of the camera, have been elucidated in S. Deep *et al.*[37] Fig. 4 shows a descriptive block diagram of various steps involved in obtaining the 2D temp field near the model, starting from the camera calibration. The steps may be frozen into four major ones: (1) Camera calibration; (2) Image acquisition; (3) Image post-processing; and (4) Presentation of results.

ACCEPTED MANUSCRIPT

AIP Publishing

This manuscript was accepted by Phys. Fluids. Click here to see the version of record.

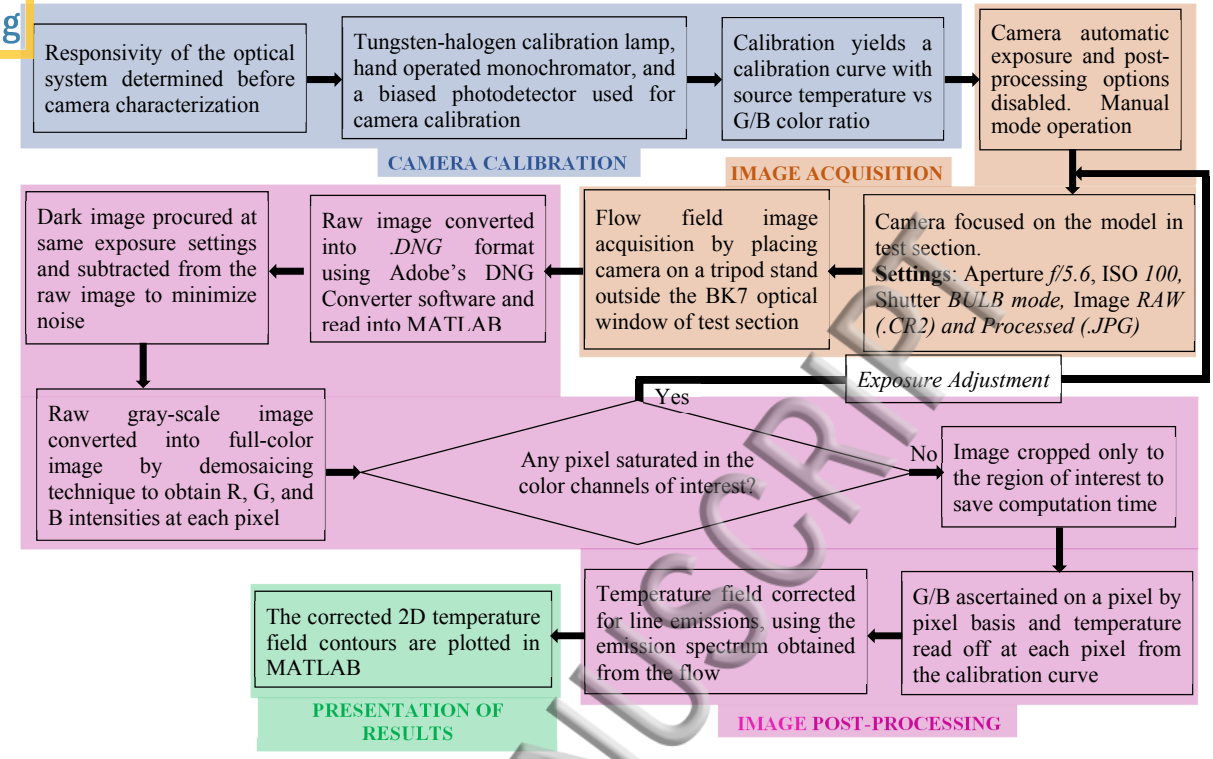

FIG. 4. Block diagram of steps involved in obtaining 2D temperature field starting from camera calibration.

E. Emission spectrum from the shock layer

The emission spectrum obtained from the radiating gaseous species in the shock layer is predominantly continuous broadband in nature. However, over and above this are superimposed strong emission lines at discrete wavelengths, occurring due to radiative transition. This causes a systematic error in the temperature estimated by TCRP as the technique assumes gray body radiation. Hence the relative contributions from these lines were ascertained and an appropriate correction was applied to obtain a more accurate temperature measurement. An Ocean Optics USB4000-FL spectrometer was used for acquiring spectra. This spectrometer uses a diffraction grating with 600 lines/mm and has a wide spectral range extending from the UV to the near infrared (350-1050 nm). It has a signal-to-noise ratio of 300:1 at full signal. More details about the spectrometer and the correction technique may be found in S. Deep *et al*.[37]

F. Run-to-run uncertainty and error analysis of the experimental methodology

An error analysis of the experimental methodology was also performed and has been elucidated here. Two types of errors may occur during experimentation: Systematic and Random. The former affects the accuracy of a measurement and is "one-sided" as it differs from the true value by the same amount. It thus cannot be addressed by repetition of experiments and must thus be detected and reduced by refining the measurement technique. Random error, on the other hand, is "two-sided", as it fluctuates on either side of the true value. It affects the precision of the measurement and may be reduced by repeating the experiments several times.

In this paper, random errors due to run-to-run variation have been called 'experimental uncertainty' and have been indicated in parenthesis, wherever applicable. All the experiments were conducted with utmost care and repeated at least five times so as to ensure precision in the directly measured quantities, and also to ascertain shock tunnel repeatability. The average value of the measured quantities has been reported and the standard deviation about the mean mentioned as the uncertainty. For a derived quantity, the cumulative uncertainty is obtained as an RMS average of the uncertainties of all measured quantities it is dependent upon. This is the standard method of computing uncertainties and was formulated by Moffat.[43]

One of the chief sources of systematic error in TCRP is the selection of wavelength range. It was shown in a previous work that measurement in the visible regime using a DSLR camera was superior to the infrared region, by way of greater sensitivity of radiation to temperature.[44] Equipment noise also contributes to the error. Read noise would be negligible for scientific DSLR camera like ours, thermal noise due to compact camera body was taken care of by subtracting a background image, fixed pattern noise which creeps up due to inconsistency in the pixel sensitivity with sensor position was addressed by calibrating different sensor locations separately and the maximum difference in G/B ratio for any temperature was about 0.5% and hence neglected. Dust deposition on the optical window may be

ACCEPTED MANUSCRIPT

AIP Publishing

another cause of systematic error and was therefore taken into account during camera calibration by making the window a part of the set-up. Apart from this, since the camera yields discrete signal levels, an average spatial error of ±0.5% in signal was estimated in the intensity count for each discrete wavelength.[45] This led to a modified calibration curve. Then, the modified green and blue levels captured during the actual experiment were used to evaluate a new G/B ratio and the temperature read off from the calibration curve. This was compared to the actual temperature and error was reported. The particular combination of $[C_G + 0.5\%C_G, C_B - 0.5\%C_B]$ yielded the maximum absolute error of 2% on the measured temperature. C_G and C_B are counts obtained from the camera in the green and blue channel respectively.

As far as the heat flux measurements are concerned, one of the sources of error is the thickness of the platinum gauge which was assumed to be zero in obtaining the working equation from the governing transient 1D equation. It may be proved that[41]

$$\frac{\dot{q}}{\dot{q}_0} = 1 - \frac{1}{\sqrt{\pi} z}\left(\frac{1}{a} - \frac{a}{2}\right) \quad (3)$$

where $\dot{q}$=deduced heat flux rate with thickness equal to zero, $\dot{q}_0$=actual heat flux rate, z=$\sqrt{\alpha_1 t}/l$, l=thickness of gauge, a=$(\rho_2 c_2 k_2/\rho_1 c_1 k_1)^{0.5}$, subscript 1 refers to platinum and 2 refers to Macor substrate. For l=1 μm and t=315 μsec (steady test time), plugging in the value of a for our case yields $\dot{q}/\dot{q}_0$~0.97, i.e., an absolute error of 3%. It was also noted that heat flux rates may be subject to errors as much as 10% if substrate temperature went up by 150 ºC. Also, if assumption of 1D conduction is not strictly valid and 2D conduction occurs, measured temperature is reduced by a factor of $(1 - \sqrt{\alpha_1 t}/2w\sqrt{\pi})$,[41] w being the width of the film and equal to 2 mm. In our case, this simplifies to an absolute error of 7% from the true value.

III. RESULTS AND DISCUSSIONS

A. Flow conditions

A 3 mm thick aluminum sheet placed between the driver and the driven sections served as the primary diaphragm. The diaphragm had two mutually perpendicular grooves, 0.75 mm deep, and had a bursting pressure of 10 MPa (± 3%). Helium was used as the driver gas and filled to a pressure of 700 torr (0.093 MPa) in the compression tube. The shock tube was filled with atmospheric air at a pressure of 165 torr (0.022 MPa). Run-to-run variation of initial fill pressure of the compression tube was ± 1.88% and that of driven tube was 0.7%. The incident shock speed was measured to be 2515 m/sec (Mach 7.24), with a run-to-run variation of ± 2%. The measured stagnation pressure (nozzle supply pressure) was 8 MPa (± 2%). The stagnation conditions obtained behind the reflected shock were estimated using the shock tube and nozzle calculations numerical code (STN),[46] which takes into account 'real-gas effects'. The stagnation conditions behind the reflected shock, obtained from STN are given in Table I. They are denoted by a suffix 'stag'.

TABLE I. Stagnation conditions from STN

Temperature T_{stag} (K) [± 2.1%]	4123
Enthalpy h_{stag} (MJ/kg) [± 2.2%]	6.31
Density ρ_{stag} (kg/m^3) [± 2.4%]	6.23

Another code, STUBE 2.5,[47] was used to predict nozzle-exit (free stream) conditions, taking chemical non-equilibrium into account. STUBE is a one-dimensional inviscid simulation of the shock tunnel nozzle flow, modeling both vibrational and rotational temperatures. The code predicts a variation of flow field quantities and species along the length of the nozzle and calculates the nozzle exit conditions for the conical nozzle, taking chemical non-equilibrium into account. STUBE requires nozzle geometric coefficients as an input, which are measured for the HST3 and provided to the code. Tabulated below are the free stream conditions obtained from the code, denoted by a suffix '∞'.

TABLE II. Free stream conditions from STUBE

Mach number M_∞ [± 1.1%]	9.84
Static pressure P_∞ (Pa) [± 2.5%]	200.38
Static temperature T_∞ (K) [± 2.2%]	289.68
Static density ρ_∞ (kg/m^3) [± 2.1%]	0.0024
Velocity U_∞ (m/sec) [± 2.1%]	3273
Reynolds number Re_∞ (million/m) [± 6%]	0.43

Fig. 5 shows the pressure signal obtained from the P5 pressure transducer mounted on the shock tube closest to the paper diaphragm and that from the pitot pressure transducer mounted just below the test model in the test-section. The P5 transducer shows two sharp jumps, marked 1 and 2. The former is due to the incident shock and the latter due to the reflected shock. It shows a steady nozzle supply time of approximately 340 μsec. The pitot pressure transducer signal, amplified considerably for easy visualization, yields a steady flow time of about 315 μsec. The steady pitot signal has been highlighted in light grey.

B. Effect of Cr coating on shock layer temperature

The calibration of the camera yields a temperature versus intensity ratio for each color channel (R, G and B) combination. Fig. 6 shows the calibration curves that relate temperature with the R/G and G/B ratios. It may be noted from the figure that for the range of temperatures expected for our experiments (>3000 K), the G/B ratio is more sensitive to temperature changes compared to its R/G counterpart, which becomes asymptotic to the abscissa. Hence, we use the green/blue intensity ratio for temperature characterization in the shock layer.

The 2D, spatially resolved temperature field characterization of the shock layer formed in the proximity of the model was done, first without any coating over the model. Emission spectroscopy performed in the test section, as described earlier, helps

ACCEPTED MANUSCRIPT

AIP Publishing

This manuscript was accepted by Phys. Fluids. Click here to see the version of record.

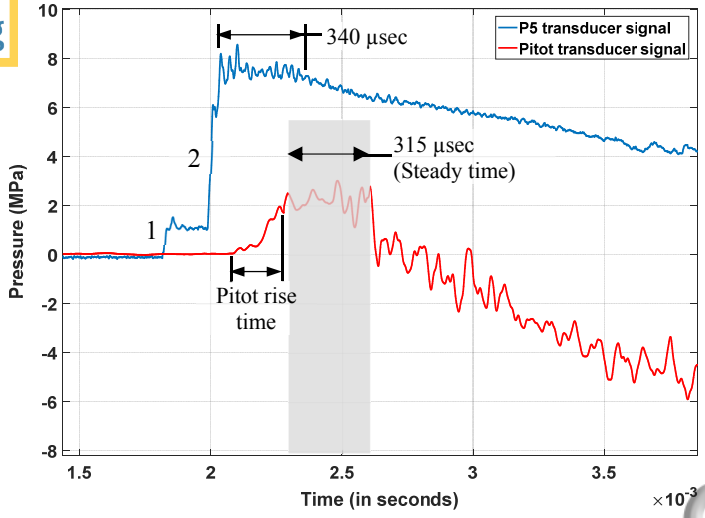

FIG. 5. Pressure transducer signals. The pitot sensor yields a steady test time of about 315 µsec, highlighted in grey.

correct for discrete lines superimposed over the continuous broadband emission. Correction yielded approximately a 50 K (1.67%) increase in temperatures above 3000 K. The temperature in the stagnation region, after correcting for line emissions was found to be 3369 K (run-to-run variation: ± 1%). Theoretical uncertainty in temperature measurement due to uncertainties in camera digitization, calibration, pixel resolution, pixel noise, etc. was calculated to be ± 4%.

After completion of a set of experiments, the surface of the model (aluminum) was coated with a thin film of 99% pure Cr and the experiments were repeated. TCRP yielded a stagnation region temperature of 3542 K (± 0.99%), after line emission correction. This is a 173 K (about 5%) increase from its uncoated counterpart.

Fig. 7(a) shows the JPEG image of the flow over the model (inset), along with the processed 2D temperature field (corrected for line emissions) for the case of no Cr coating. The nose of the model is outlined in white, determined from edge detection algorithms. Since it is difficult to determine the stagnation point, an average

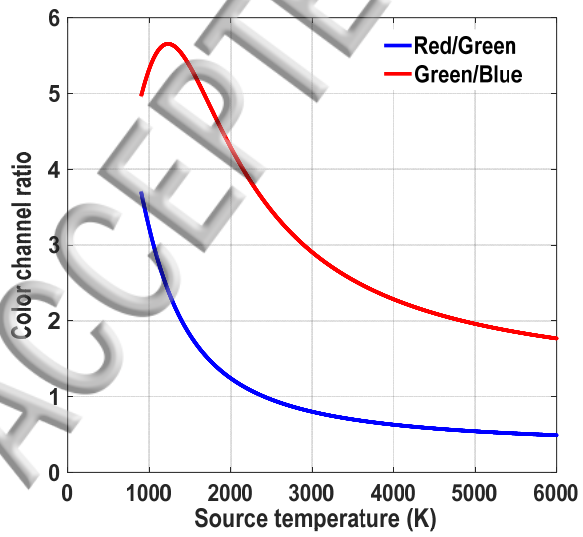

FIG. 6. Calibration curves- Color channel ratio vs source temperature.

temperature was calculated in the stagnation region marked by a square (black) 12 pixels by 12 pixels. Due to the 3D nature of the bow shock formed in front of the model, it encapsulates the entire model surface and hence portions of the model behind the white line seem illuminated in the figure.

It must be noted here that although temperature increase has been reported only close to the stagnation point, the entire surface of the model was coated with Cr. A question naturally arises if Cr oxidation from regions away from the stagnation zone has a role to play in the temperature augmentation in that region. To address the question, experiments were repeated on a new model with Cr coated only in the sonic circle (determined from computations), a circular region around the model stagnation point within which the flow is subsonic and the effect of the bow shock on physical quantities the strongest. Calculations helped procure a stagnation temperature of 3553 K (± 1%) as shown in Fig. 7(b), in close agreement with the previous value of 3542 K, confirming that the rise in temperature in the stagnation region is due to the oxidation of Cr coated near the model stagnation point (within the sonic circle) only.

The emission spectrum obtained from the test section due to the radiating gaseous species present in the shock layer has been shown in Fig. 8. It is evident that the spectrum is predominantly broadband and the two strong radiative transition lines in the spectrum occur near 590 nm and 777 nm, which, according to the literature, are caused due to emission from Na atoms and atomic oxygen in the flow.[48-50] The emission spectrum thus confirms the presence of atomic oxygen in the flow, imperative for Cr oxidation. Since the latter falls outside the bounds of camera's spectral response curve (visible region, 400-700 nm), only the correction for the former needs to be performed.

ACCEPTED MANUSCRIPT

AIP Publishing

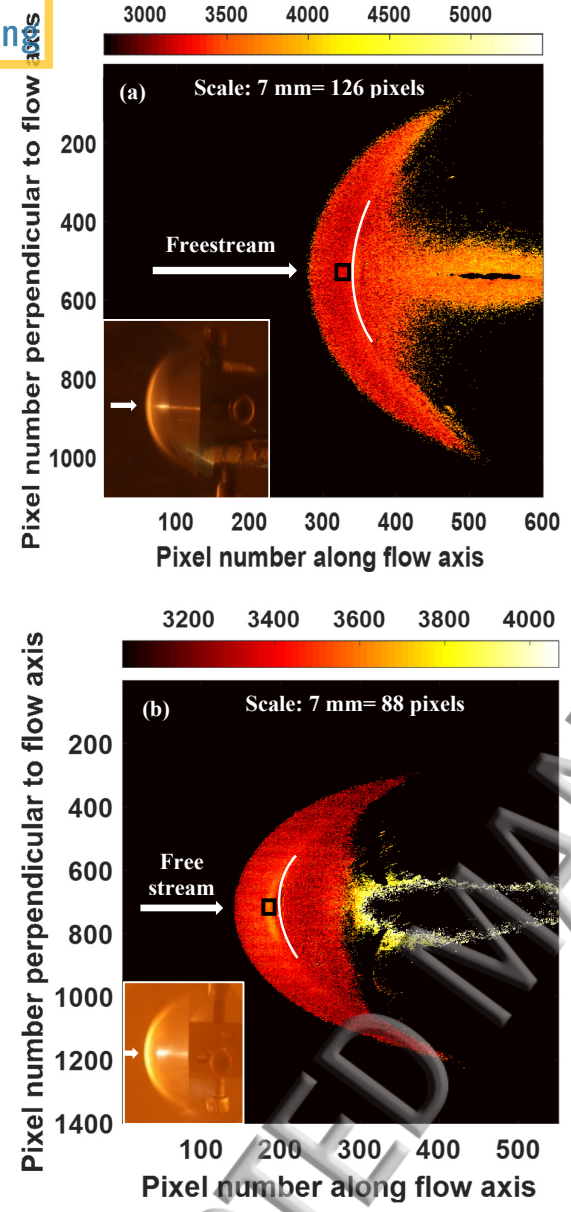

FIG. 7. 2D temperature distribution in the shock layer. (a) Uncoated surface; (b) With Cr coating in sonic circle. Inset- Respective photograph of flow over the models. Stagnation region temperature in (b) is about 173 K more than that in (a).

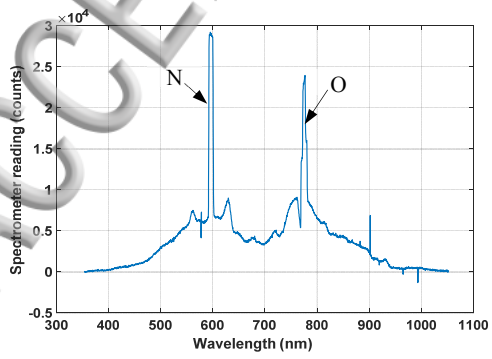

FIG. 8. Emission spectrum obtained from the test section of HST3. Discrete emission lines occur at 590 nm and 777 nm.

C. Effect of Cr coating on heat flux on the model surface

Heat flux measurements were done first over the uncoated model surface at each gauge location, with average value during the test time calculated. Pt thin film heat transfer gauges have a response time of the order of 5 µsec and are suitable for measurements in impulse facilities with short test times. The heat flux values obtained at each of the five gauge locations, averaged during the steady test time, is given below in Table III. The overall measurement uncertainty of heat flux with the thin film technique is calculated at approximately ± 6%, which is an RMS value of the directly measured quantities it is derived from. Since heat flux also happens to be an experimentally measured quantity, the run-to-run variations have been mentioned in brackets. The surface heat flux is maximum at the stagnation point and progressively reduces as one moves away from it.

TABLE III. Heat flux at gauge locations

Gauge no.	Avg. heat flux (W/cm^2) on uncoated model	Avg. heat flux (W/cm^2) on Cr coated model
1 (stagnation pt)	122.11 (± 2.3%)	153.34 (± 2.7%)
2	81.1 (± 2.8%)	85.09 (± 1.7%)
3	68.44 (± 2.7%)	71.64 (± 1.7%)
4	45.5 (± 2.1%)	47 (± 1.2%)
5	37.77 (± 1.9%)	38.89 (± 1.3%)

The experiments were repeated with the entire model surface coated with Cr. The stagnation point heat flux thus obtained was 153.34 W/cm^2 (± 2.7%), a 26% increase from that over the uncoated model. Convective heat flux for the rest of the surface, away from the stagnation point, did not show any considerable increase from their uncoated counterpart, as evident from Table III. The trend was similar for the gauges on the other side, i.e., 2a-5a. Since gauges 2-5 lie outside the sonic circle of the model, they only see an oblique shock whose gas layer heating effect is too little to cause effective Cr oxidation. Hence the effect of Cr presence is negligible in those locations. Fig. 9 shows the heat flux signals obtained at the stagnation point gauge, with and without Cr coating. The steady test time of 315 µsec, used for reporting the average value of heat flux has been highlighted in light grey.

To complement the experimental results obtained on the uncoated model, detailed numerical simulations were performed in ANSYS Fluent 14.5 CFD package, modeling air dissociation in the shock layer occurring at high stagnation enthalpies. The accuracy of any simulation depends on the modeling and formulation of the physics of the problem.

Thorough finite rate chemistry was setup for external hypersonic flow in Fluent. Fluent workbench was used for the entire simulation, starting from the geometry design right up to the post-processing of results. A 2D, axisymmetric geometry was created to save computational cost and the flow-domain discretized

ACCEPTED MANUSCRIPT

AIP Publishing

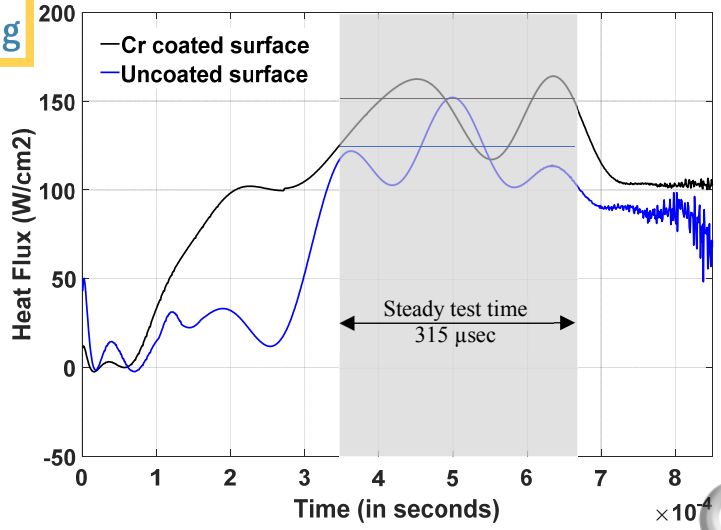

FIG. 9. Heat flux signals at the stagnation point. The steady test time of 315 µsec has also been highlighted in light grey. Avg. heat flux values in the steady test time have been marked by a horizontal line.

with 245,000 elements. After obtaining the solution with the normal mesh, a solution-adaptive pressure- gradient based grid refinement was adopted, with a refined threshold of 10% of the maximum pressure value. This was repeated until no additional iterations were required to converge the solution between each relative grid. This is done mainly to improve the numerical accuracy in regions across the shock front, which witness large jumps in flow field quantities.

A density based, steady-state solver with absolute velocity formulation was used, with the energy equation turned on for compressible flow. 2D Reynolds-averaged Navier-Stokes (RANS) equations were utilized to numerically simulate the flow field. The shear stress transport (SST) k-ω turbulent model[51] is employed, with species transport checked as a tool to predict the chemical reactions and species concentration in the shock layer. The SST model has been proved to be quite suitable for chemically reacting boundary layer problems involving near-wall dissociation and is also insensitive to the initial free stream values.[52] The Eddy-Dissipation Concept (EDC) model[51] (turbulence-chemistry interaction) was used for computing the reaction rates that appear as source terms in the chemical species conservation equation. The computational studies were carried out for air as the test gas. A 5-species (*NO, N, O, O_2 and N_2*), 17-reaction model (including third body (M) reactions) has been used for the computations. The number of flow iterations per chemistry update was set to 5. C_p was assumed to be piecewise-linear for each species, with values obtained from NASA polynomials.[53] Mixing law formulation for C_p, thermal conductivity (k) and viscosity (μ) was used for the bulk gas. The inputs to the Arrhenius rate equation (4), required for calculation of the forward rate constant for each reaction, were obtained from the NIST Database.[54]

$$k_f = AT^{\beta} exp(-E/RT) \qquad (4)$$

where k_f=forward rate constant, A=pre-exponential factor, β=temperature exponent, E=activation energy for the reaction and R=universal gas constant.

Appropriate boundary conditions (BCs) were assigned to the fluid domain. Conjugate heat transfer was considered, with the aluminum solid modeled. An implicit formulation, AUSM flux type and a second-order spatial discretization were used as solution methods for improved accuracy. An absolute convergence criterion was used, and the simulation was run until all the residuals fell to at least 1×10^{-06}. The drag coefficient (C_d) on the wall was simultaneously monitored and plotted on the graphics window, a constant value indicating convergence. The flow field was initialized with the free-stream conditions obtained from another code, mentioned in Section III A. The modeled reactions have been mentioned in Table IV.

TABLE IV. 17-reaction model for computations

Reaction Name	Reaction	Third bodies
O_2 dissociation	$O_2 + M = 2O + M$	O_2, N_2, NO, O, N
N_2 dissociation	$N_2 + M = 2N + M$	O_2, N_2, NO, O, N
NO dissociation	$NO + M = N + O + M$	O_2, N_2, NO, O, N
N_2-O exchange	$N_2 + O = NO + N$	-
NO-O exchange	$NO + O = N + O_2$	-

D. Heat flux comparison with numerical simulations and analytical expressions

In addition to complementing the experimental heat flux values on the uncoated model with appropriate numerical simulations, analytical expressions by Lester Lees[38] for surface heat transfer rate distribution over blunt cone were also used. Separate expressions for the ratio of surface heat flux at a surface location to the stagnation point heat flux are given for the nose and the conical skirt, as functions of the angular position of the location on the surface, radius of the spherical nose, and free stream gamma (ratio of specific heats) and Mach number.

The classic Fay and Riddell expression[39] was also employed to predict the stagnation point heat flux.

ACCEPTED MANUSCRIPT

AIP Publishing

This manuscript was accepted by Phys. Fluids. Click here to see the version of record.

$$\dot{q}_s = 0.763 Pr^{-0.6} (\rho_e \mu_e)^{0.4} (\rho_w \mu_w)^{0.1} C_p (T_0 - T_w) \sqrt{\left(\frac{du}{ds}\right)_0} \quad (5)$$

where Pr=Prandtl number, ρ=density, μ=dynamic viscosity, T=temperature and C_p=specific heat at constant pressure. All these properties correspond to air. The subscript 'e' refers to values of a physical quantity at the outer edge of the boundary layer formed in front of the model, 'w' refers to those on the wall of the test model. T_0 is the total (stagnation) temperature. $(du/ds)_0$ is the stagnation point velocity gradient and for a modified Newtonian flow, it is given by

$$\left(\frac{du}{ds}\right)_0 = \frac{1}{R}\sqrt{\frac{2(p_e - p_\infty)}{\rho_e}} \quad (6)$$

where R=nose radius, p=pressure and '∞' refers to the free stream condition. The pressure at the boundary layer edge, p_e, may be related to the free stream pressure, p_∞ by the following relation. A comprehensive proof of the relation is given in the Appendix.

$$p_e = p_\infty \left[\frac{(\gamma+1)^2 M^2}{4\gamma M^2 - 2(\gamma-1)}\right]^{\frac{\gamma}{\gamma-1}} \left[\frac{2\gamma M^2 - \gamma + 1}{\gamma+1}\right] \quad (7)$$

The measured temperature of 3369 K was used as the total temperature. A standard value of 0.71 was taken as the Prandtl number for air. The free stream Mach number and pressure were taken from Table II. The three coefficient Sutherland's law (μ_0=1.716×10^{-5} kg/m-sec, T_{ref} =273.15 K and S_{air}=110.4 K) was used to compute the dynamic viscosity. The nose radius, as stated before, was 30 mm. Since the variation of temperature from the boundary layer edge to the model wall is large (3369 K to ~300 K), the variation of C_p will likewise be considerable. Hence, the value of C_p was taken at a film temperature,[55] equal to the mean of the stagnation point temperature and wall temperature. The corresponding value was 1240 J/kg-K.

The calculations yielded a Fay-Riddell heat flux of 125.11 W/cm^2 (± 2.9%), in close agreement with the experimentally obtained value of 122.11 W/cm^2. Fig. 10 is a consolidated plot of the experimental, computational and analytical heat flux over the model without Cr coating. The experimental heat flux values with the Cr film have also been included. The graph shows the heat flux values at all the 9 gauge locations (1, 2-5 and 2a-5a). A schematic of the model with the gauge locations and the flow direction has also been shown.

E. Effect of Cr coating on stagnation point shock stand-off distance

We have measured shock stand-off in our experiments using a standard Z-type Herschellian Schlieren system[56] and an intensity-scan (horizontally across the shock layer) based method from the DSLR camera RGB image and corroborated them with computational measurements.

A standard Canny edge detection algorithm[57] performed on the schlieren image obtained during the steady test time for flow on the uncoated model yielded a stand-off distance of 3.82 mm (± 1.4%). The intensity-scan based method (described in the next paragraph) using the full-color *.jpeg image from the DSLR camera yielded a stand-off distance of 3.65 mm (± 1.8%). The corresponding value from computations was 3.68 mm.

For the experiments on the Cr coated surface, the edge detection algorithm performed on the gray scale schlieren image obtained during the steady test time yielded a stand-off distance of 4.45 mm (± 1.5%). The edge detection image is shown in Fig. 11. It is a binary image with the edges in white stored as 1 and the rest of the black space stored as 0. A horizontal intensity scan yields the shock stand-off distance in pixel count. An appropriate calibration of the image relating the pixel count to a known dimension yields the actual shock stand-off distance. A similar technique, using the color

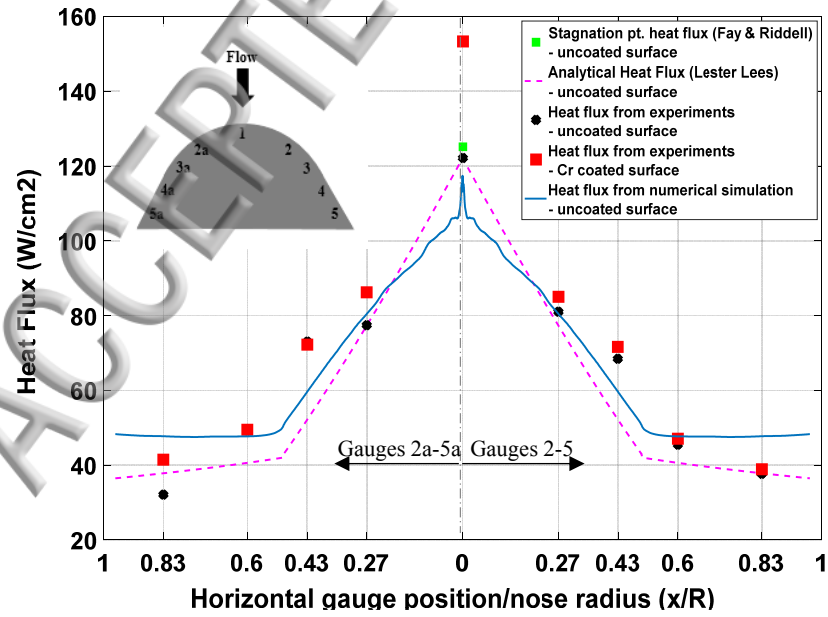

FIG. 10. Heat flux comparison on the entire model surface-experimental, computational, and analytical.

ACCEPTED MANUSCRIPT

This manuscript was accepted by Phys. Fluids. Click here to see the version of record.

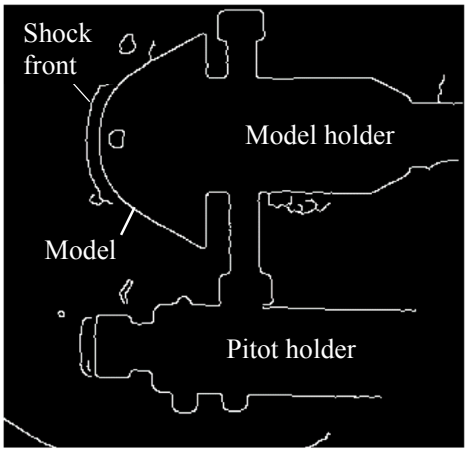

FIG. 11. Canny edge detection performed on the schlieren image of flow over the Cr coated surface. Shock stand-off distance=4.45 mm.

image of the flow taken from the DSLR camera, was also used to predict the stand-off distance. The RGB image was intensity-scanned along a line shown in Fig. 12(a) in the R and B color channels separately. Fig. 12(b) shows the variation in intensity along the line in each of the color channels. The pixel number on the blue intensity curve (marked 1) beyond which the change in intensity (>3.6%) becomes significantly greater than the preceding changes is taken as the stagnation point on the model surface. The red intensity curve reaches saturation (and remains constant) for pixels lying inside the shock layer and then begins to descend, as evident from the figure. The pixel number (marked 2) after which the drop is less steep is chosen as the end of the shock layer. The points have been marked in Fig. 12(b). The distance between pixels 1 and 2 gives the shock stand-off distance, which may be converted into dimensions of length after an appropriate calibration. The stand-off distance thus calculated was 4.34 mm (± 2%). It may be noted that since the camera's in-built software performs a lot of post-processing including brightness enhancement for aesthetically pleasing images, the *.jpeg images are saturated. The raw images were unsaturated, however, and facilitated temperature characterization. A summary of the shock stand-off distances is given in Table V. Therefore, the presence of Cr film over the model surface pushes the shock away from the nose, thereby increasing shock stand-off distance by about 17%.

Table V. Shock stand-off distance

Shock stand-off distance	From DSLR camera full-color image (mm)	From Schlieren image (mm)	Computations (mm)
Uncoated	3.65 (±1.8%)	3.82 (±1.4%)	3.68
Cr coated	4.34 (±2%)	4.45 (±1.5%)	-

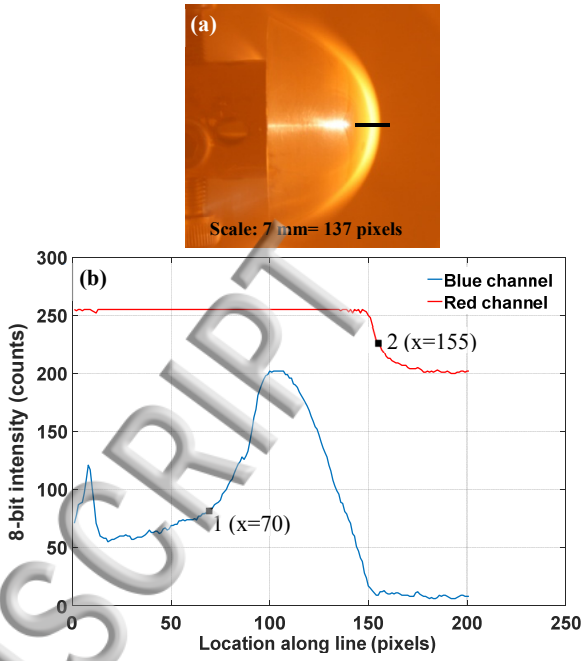

FIG. 12. Shock stand-off distance for Cr coated model from the DSLR *.jpeg image. (a) Image of the flow over the model. Intensity scan is performed along the black horizontal line from left to right; (b) Intensity scan in the blue and red channel. Body stagnation point marked 1 (pixel 70) and point on shock front marked 2 (pixel 155). Shock stand-off distance=4.34 mm.

F. Chromium oxidation kinetics- Estimation of energy deposition due to Cr oxidation and its distribution

Analytical calculations were performed to study Cr oxidation kinetics- to estimate the total energy deposited in the shock layer due to Cr oxidation and elucidate its distribution in various processes. The global one-step chromium/air reaction is as follows:[14]

$$2Cr + O_2 = 2CrO + Heat \quad \text{(Global reaction)}$$

Enthalpy of formation of Cr (g) and CrO is 397 kJ/mole and 186 kJ/mole respectively.[58] Enthalpy of the global reaction is therefore -211 kJ/mole, negative sign indicating an exothermic reaction. The reactions shown above indicate that the presence of nascent oxygen [O] in the shock layer is indispensable to the oxidation of Cr. Contours of mole fraction of [O] obtained from numerical computations have been shown in Fig. 13, indicating a healthy concentration of atomic oxygen in the gas layer, close to the coated surface.

Molar mass of CrO being 68 gm, energy released/mass is 3100 J/gm. The Cr regression rate in the stagnation region is 0.05 mm/sec.[14] Although the stagnation enthalpy in the referred article is slightly different from ours, the Cr recession rate computed served as a good starting point and has as such been used in this paper. Additionally, a first order estimation was performed to obtain the recession rate based on the electrical resistance of a small portion of the model with and without the coating. The calculation yielded a recession rate of approximately 0.054 mm/sec, thereby

ACCEPTED MANUSCRIPT

This manuscript was accepted by Phys. Fluids. Click here to see the version of record.

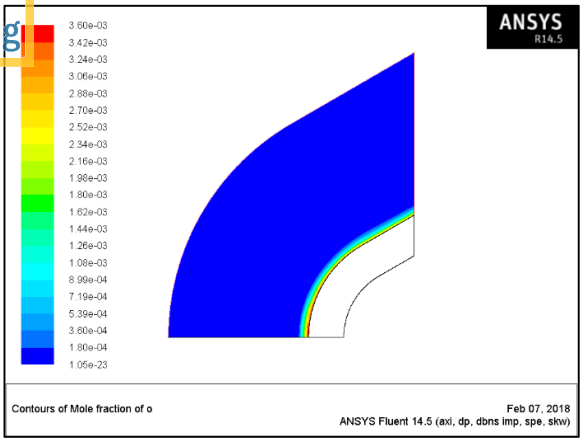

FIG. 13. Contours of mole fraction of nascent oxygen atom. High concentration close to the model surface implies effective Cr oxidation.

supporting the claim that the recession rate would not be too affected by the small difference in stagnation enthalpy. Now for an oxidation rate of 0.05 mm/sec, volume of Cr ablated/area will be 5 mm^3/sec. The density of CrO being 5.2 gm/cc, mass of CrO ablated is 0.025 gm/sec. Hence, energy released per second due to CrO formation is 78 W/cm^2 (H).

A certain portion, say Δh, is used up in pushing the shock layer away from the surface, increasing shock stand-off distance. In other words, Δh may be interpreted as the net loss of heat energy when the shock layer stands farther away from the Cr coated model surface, compared to its uncoated counterpart. Experimental results elucidated in Section III C, showed an increase in heat flux into the model surface by 31 W/cm^2, i.e., 40% of the total heat released due to oxidation is convected back into the blunt cone. The density of the dissociated air in the stagnation region is about 0.018 kg/m^3, from computations. If a cross section of 1 cm^2 of the gas layer be taken near the blunt cone wall, and if it be assumed that 1 mm of the shock layer in the stagnation region (in the axial direction) is affected by the heat dumping, the total volume of gas affected is 100 mm^3. So, the mass of gas in the region is 1.8e-09 kg. Its specific heat is 1350 J/kg-K. Since the temperature of the gas layer rises by 173 K during the test time, the net heat required for the rise is 4.2e-04 J/cm^2. The test time being 315 µsec, total energy required per second is 1.5 W/cm^2. Thus, 1.9% of the heat liberated is used up in heating the gas. Our Macor substrate thickness of 5 mm minimizes the heat loss by conduction from the rear of the substrate, to about 1% of the convective heat flux at the surface of the blunt cone. This may be proved from the expression for heat flux as a function of the depth into the substrate, obtained from the semi-infinite theory.[41] This is about 0.5% of the heat release. Also, previous computations by Tahsini[14] have shown that the radiative heat flux into the model for our enthalpy conditions amounts to about 20% of the convective heat flux, i. e., about 6.2 W/cm^2, which is 8% of the exothermic reaction heat release. Hence, summing up the heat distribution into various processes and subtracting it from the total heat released, it may be concluded that Δh=39 W/cm^2. A schematic of the heat balance is shown in Fig. 14.

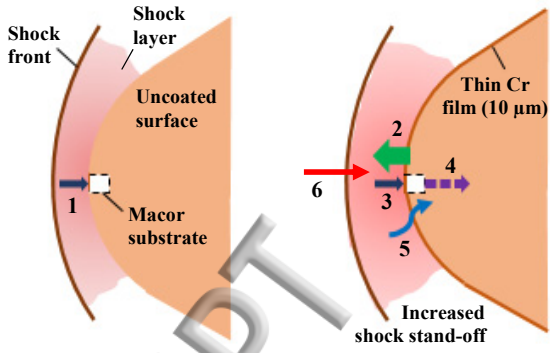

1 Convective heat flux at stag. pt. (uncoated)= 122.11 W/cm^2
2 Heat released due to Cr oxidation (H)= 78 W/cm^2
3 Convective total heat flux at stag. pt. with Cr coating= 153.34 W/cm^2
4 Heat loss from Macor rear by conduction= 0.31 W/cm^2
5 Radiative heat flux near stag. pt.= 6.2 W/cm^2
6 Heat used up in raising shock layer temp.= 1.5 W/cm^2
Heat pushing shock layer away from surface (Δh) = 2-(3-1)-4-5-6= 78-(153.34-122.11)-0.31-6.2-1.5 ~ 39 W/cm2

FIG. 14. Chromium oxidation kinetics- Distribution of released heat due to exothermic oxidation of Cr.

IV. CONCLUSIONS AND FUTURE WORK

Experiments were performed in the free-piston driven shock tunnel (HST3) at an enthalpy of 6.31 MJ/kg and a free stream Mach number of 9.84, with atmospheric air as the test gas. The key objective was to study the effect of oxidation a thin film of chromium coated over a large angle blunt cone on the thermodynamics of the shock layer formed in the vicinity of the model. The chief conclusions drawn from the study are as follows:

1. Calculations showed that oxidation of Cr in the presence of nascent oxygen atoms is a highly exothermic one, dumping 78 W/cm^2 gross heat energy into the shock layer for our enthalpy conditions. Computations and emission spectroscopy confirmed the presence of dissociated oxygen in the high enthalpy shock layer, indispensable for Cr oxidation.
2. About 1.5 W/cm^2 of the total heat released was used up in heating the gas in the stagnation region, augmenting its temperature by about 173 K. The temperature of the shock layer in the flow stagnation region was about 3369 K for the uncoated model. With Cr coating, it jumped to 3542 K.
3. Cr coating beyond the sonic circle on the model had negligible effect on the thermodynamics of the shock layer in the flow stagnation region.
4. About 31 W/cm^2 of the heat released was convected back into the test model. The net surface heat flux into the model at the stagnation point rose from 122.11 W/cm^2 for the uncoated model to 153.34 W/cm^2 for the coated counterpart.
5. Comparison of experimental heat flux on the model surface (for no Cr coating) with computational

ACCEPTED MANUSCRIPT

AIP Publishing

This manuscript was accepted by Phys. Fluids. Click here to see the version of record.

results and analytical relations by Lester Lees and Fay-Riddell showed good agreement.

6. Due to the 5 mm thick Macor substrate at the stagnation point, the heat lost by conduction from the rear of the substrate was very little, estimated to be about 0.31 W/cm^2. The radiative heat flux into the model near the stagnation point was estimated at approximately 6.2 W/cm^2.
7. The remainder of the heat liberated due to oxidation was about 39 W/cm^2. This heat had an effect of pushing the shock layer away from the model by augmenting its density, thereby increasing the shock stand-off distance by as much as about 17%. For the uncoated surface, the shock stand-off distance was experimentally measured to be 3.8 mm, while for the coated surface it was found to increase to 4.45 mm.
8. The problem of increased surface heat flux must be weighed against the advantage of drag reduction to arbitrate the feasibility of the novel idea of Cr coating in practical applications. Usage of smart thermal protection system (TPS) with self-adapting and self-healing properties, when subjected to inclement hypersonic environment, can deal with the complication of augmented heating and help qualify the simple technique of exothermic heat dumping as an effective means of drag reduction.

Future work involving usage of other test gases in the shock tunnel have been planned to see their effect on Cr film. It is expected that using pure O_2 as a test gas would result in a larger concentration of oxygen atoms in the shock layer and yield better Cr oxidation rate, thereby accentuating coating effects. Further, argon being a noble gas, its usage as a test gas should have little effect on Cr coating. In this paper, the regression rate of Cr was taken from results of numerical computations performed for close enthalpy conditions in a different literature.[14] Direct measurement of Cr ablation rate through depth profiling using X-ray photoelectron spectroscopy (XPS) will be attempted next. Morphological and compositional analysis of the thin Cr film, using advanced techniques such as XRD and SEM-EDS will be done in the future to determine the changes in chemical composition at the surface and sub-surface level of the coating. Detailed numerical simulations modeling chromium oxidation will also be performed as an alternative means of knowing the recession rate.

ACKNOWLEDGEMENTS

We would like to thank Jeevan, N Kumar, and Gangadhar Murthy for their help in performing the experiments. Technical discussions with Tarandeep Singh and Dr. Yedhu Krishna, colleagues in the laboratory, have helped give this work a better shape. Financial support by DRDO, India, is acknowledged.

APPENDIX

PROOF OF THE RELATIONSHIP BETWEEN FREE STREAM PRESSURE (p_∞) AND BOUNDARY LAYER EDGE PRESSURE (p_e)

Flow over a blunt body under hypersonic conditions results in the formation of a strong, detached bow shock. Fig. 15 is a schematic of the flow field over a blunt vehicle such as that used for our experiments. The body wall (w), outer edge of the boundary layer (e), the free stream region just ahead of the shock (∞) and the region just behind the shock but ahead of the boundary-layer (2) have been marked in the figure. The stagnation streamline has also been shown. The dimensionless velocity boundary-layer (BL) thickness (δ_2/D) for such flows varies as $Re_D^{-1/2}$, where Re_D is the post-shock Reynolds number and may be related to the free stream Reynolds number, $Re_{D,\infty}$ approximately as $Re_D \approx Re_{D,\infty}/M_\infty$.[59]

For our case of high free stream Reynolds number of 0.43 million/m, the BL thickness will be very small, and it will be extremely close to the body wall. For the proof, then, the Mach number at the point of intersection of the BL edge and the stagnation streamline has been assumed to be zero (M_e=0), due to its vicinity to the stagnation point.

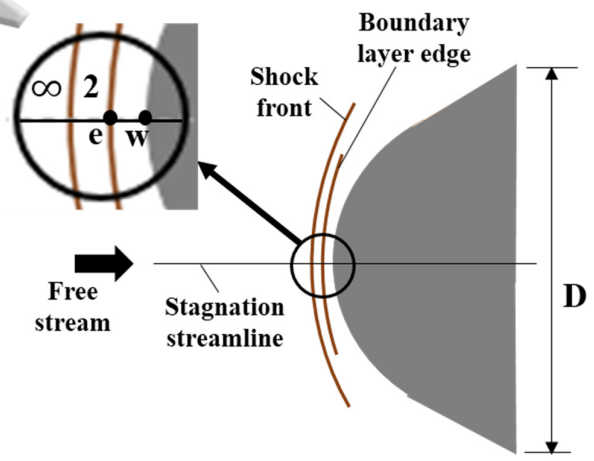

FIG. 15. Schematic of the flow field over a blunt vehicle.

Then,

$$p_e = \left(\frac{P_e}{P_{0e}}\right)\left(\frac{P_{0e}}{P_{02}}\right)\left(\frac{P_{02}}{P_{0\infty}}\right)\left(\frac{P_{0\infty}}{P_\infty}\right)p_\infty \qquad \text{(A1)}$$

Terms with a subscript '0' refer to stagnation conditions.

$\frac{P_e}{P_{0e}} = 1$ (since Mach number at 'e' is assumed to be 0)

$\frac{P_{0e}}{P_{02}} = 1$ (since the region between the shock front and BL edge is isentropic)

Substituting expressions for the ratio of stagnation pressures across a shock ($P_{02}/P_{0\infty}$) and the ratio of stagnation pressure to static pressure at a point ($P_{0\infty}/P_\infty$) as a function of the free stream Mach number (M), we have:

ACCEPTED MANUSCRIPT

AIP Publishing

$$p_e = \left[\left(\frac{\frac{\gamma+1}{2}M^2}{1+\frac{\gamma-1}{2}M^2}\right)^{\frac{\gamma}{\gamma-1}}\left(\frac{2\gamma M^2-\gamma+1}{\gamma+1}\right)^{-\frac{1}{\gamma-1}}\right]\left[1+\frac{\gamma-1}{2}M^2\right]^{\frac{\gamma}{\gamma-1}}p_\infty \quad \text{(A2)}$$

Rearranging and simplifying,

$$p_e = \left[\left(\frac{\gamma+1}{2}M^2\right)^{\frac{\gamma}{\gamma-1}}\left(\frac{\gamma+1}{2\gamma M^2-\gamma+1}\right)^{\frac{1}{\gamma-1}}\right]p_\infty \quad \text{(A3)}$$

$$= \left[\left(\frac{\gamma+1}{2}M^2\right)^{\frac{\gamma}{\gamma-1}}\left(\frac{\gamma+1}{2\gamma M^2-\gamma+1}\right)^{\frac{\gamma}{\gamma-1}-1}\right]p_\infty \quad \text{(A4)}$$

or, $$p_e = p_\infty\left[\frac{(\gamma+1)^2M^2}{4\gamma M^2-2(\gamma-1)}\right]^{\frac{\gamma}{\gamma-1}}\left[\frac{2\gamma M^2-\gamma+1}{\gamma+1}\right] \quad \text{(A5)}$$

[1]Anderson Jr, J.D., 2000. Hypersonic and High Temperature Gas Dynamics (pp. 321-332). AIAA Publications, AIAA, Reston, VA.
[2]R. K. Lobb, "Experimental measurement of shock detachment distance on spheres fired in air at hypervelocities," AGARDograph 68 Elsevier, 519-527 (1964).
[3]Ellinwood, J.W. and Mirels, H., 1968. Axisymmetric hypersonic flow with strong viscous interaction. Journal of Fluid Mechanics, 34(4), pp.687-703.
[4]Bertram, Mitchel H. "Hypersonic laminar viscous interaction effects on the aerodynamics of two-dimensional wedge and triangular planform wings." (1966).
[5]D. J. Maull, "Hypersonic flow over axially symmetric spiked bodies," Journal of Fluid Mechanics **8**, 584-592 (1960).
[6]S. M. Bogdonoff, and I. E. Vas, "Preliminary investigations of spiked bodies at hypersonic speeds," Journal of the Aerospace Sciences **26**, 65-74 (1959).
[7]Venukumar, B., Jagadeesh, G. and Reddy, K.P.J., 2006. Counterflow drag reduction by supersonic jet for a blunt body in hypersonic flow. Physics of fluids, 18(11), p.118104.
[8]W. Huang, J. Liu, and Z. X. Xia, "Drag reduction mechanism induced by a combinational opposing jet and spike concept in supersonic flows," Acta Astronautica **115**, 24-31 (2015).
[9]K. Satheesh, and G. Jagadeesh, "Effect of concentrated energy deposition on the aerodynamic drag of a blunt body in hypersonic flow," Phys. Fluids 19, 031701 (2007).
[10]M. Viren, S. Kumar, T. Maruta, K. P. J. Reddy, and K. Takayama, "Hypersonic flow over a multi-step afterbody," Shock Waves **14**, 421 (2005).
[11]F. Maurer, and W. Brungs, "Influencing the drag and the bow wave by a heat addition in the stagnation point domain of blunt bodies in supersonic flow," VI International Congress of Flight Sciences (ICAS), Munich, Germany, Sept. 9-13 (1968).
[12]J. P. Reding, and D. M. Jecmen, "Effects of external burning on spike induced separated flows," J. Spacecr. Rockets **20**, 452 (1983).
[13]G. R. Srinivasan, and R. R. Chamberlain, "Drag reduction of spiked missile by heat addition," AIAA, Atmospheric Flight Mechanics Conference and Exhibit, 4714 (2004).
[14]A. M. Tahsini, "Heat release effects on drag reduction in high speed flows," International Journal of Heat and Mass Transfer 57(2), 657-61 (2013).
[15]M. Shneider, " Energy addition into hypersonic flow for drag reduction and steering," in Atmospheric Pressure Weakly Ionized Plasmas for Energy Technologies, Flow Control and Materials Processing, Princeton, NJ, August 22-24 (2011).
[16]C. Cai and X. He, " Energy deposition/extraction effects on oblique shock waves over a wedge," AIAA Journal **45**(9), 2267–2272 (2007).
[17]F. Marconi, " An investigation of tailored upstream heating for sonic boom and drag reduction," 36th AIAA Aerospace Sciences Meeting and Exhibit, 333, (1998).
[18]D. Riggins, H. Nelson, and E. Johnson, " Blunt-body wave drag reduction using focused energy deposition," AIAA Journal **37**(4), 460–467 (1999).
[19]K. Kar, S. Roberts, R. Stone, M. Oldfield, and B. French, "Instantaneous exhaust temperature measurements using thermocouple compensation techniques," SAE Technical Paper, No. 2004-01-1418, (2004).
[20]R. W. Bilger, Instrumentation for Flows with Combustion, A. M. K. P. Taylor Academic, London, 1-51 (1993).
[21]P. C. Miles, and F. C. Gouldin, "Determination of the time constant of fine-wire thermocouples for compensated temperature measurements in premixed turbulent flames," Combustion science and technology **89**(1-4), 181-199 (1993).
[22]P. A. Bejarano, and Y. A. Levendis, "Single-coal-particle combustion in O2/N2 and O2/CO2 environments," Combustion and flame **153**(1-2), 270-287 (2008).
[23]F. Cignoli, S. De Iuliis, V. Manta, and G. Zizak, "Two-dimensional two-wavelength emission technique for soot diagnostics," Applied Optics **40**(30), 5370-5378 (2001).
[24]T. Fu, H. Zhao, J. Zeng, M. Zhong, and C. Shi, "Two-color optical charge-coupled-device-based pyrometer using a two-peak filter," Rev. Sci. Instrum. **81**, 124903 (2010).
[25]J. R. Branstetter, "Some practical aspects of surface temperature measurement by optical and ratio pyrometers," Technical Note TND-3604, NASA (1966).
[26]H. Ma, R. Stevens, and R. Stone, "In-cylinder temperature estimation from an optical spray-guided DISI engine with color-ratio pyrometry (CRP)," SAE Technical Paper, No. 2006-01-1198, (2006).
[27]F. Zander, "Surface temperature measurements in hypersonic testing using digital single-lens reflex cameras," Journal of Thermophysics and Heat Transfer **30**(4), 919-925 (2016).
[28]Z. W. Jiang, Z. X. Luo, and H. C. Zhou, "A simple measurement method of temperature and emissivity of coal-fired flames from visible radiation image and its application in a CFB boiler furnace," Fuel **88**(6), 980-987 (2009).
[29]F. S. Billig, "Shock-wave shapes around spherical-and cylindrical-nosed bodies," Journal of Spacecraft and Rockets **4**(6), 822-823 (1967).
[30]W. E. Moeckel, "Approximate method for predicting form and location of detached shock waves ahead of plane or axially symmetric bodies," Technical Note 1921, NACA (1949).
[31]C. Y. Wen, and H. G. Hornung, "Non-equilibrium dissociating flow over spheres," Journal of Fluid Mechanics **299**, 389-405 (1995).
[32]F. Zander, R. J. Gollan, P. A. Jacobs, and R. G. Morgan, "Hypervelocity shock standoff on spheres in air," Shock Waves **24**(2), 171-178 (2014).
[33]R. K. Lobb, "Experimental measurement of shock detachment distance on spheres fired in air at hypervelocities," AGARDograph **68** Elsevier**,** 519-527 (1964).
[34]M. D. Van Dyke, "The supersonic blunt-body problem-review and extension," Journal of the Aerospace Sciences **25**(8), 485-96 (1958).
[35]H. Serbin, "Hypersonic Nonviscous Flow around a Sphere," Santa Monica, RAND Corporation, RM-1772, (1956).
[36]V. Kulkarni, G. M. Hegde, G. Jagadeesh, E. Arunan, and K. P. J. Reddy, "Aerodynamic drag reduction by heat addition

ACCEPTED MANUSCRIPT

AIP Publishing

This manuscript was accepted by Phys. Fluids. Click here to see the version of record.

into the shock layer for a large angle blunt cone in hypersonic flow," Phys. Fluids **20**(8), 081703 (2008).
[37]S. Deep, Y. Krishna, and G. Jagadeesh, "Temperature characterization of a radiating gas layer using digital-single-lens-reflex-camera-based two-color ratio pyrometry," Applied Optics **56**, 8492-8500 (2017).
[38]L. Lees, "Laminar heat transfer over blunt-nosed bodies at hypersonic flight speeds," Journal of Jet Propulsion **26**(4), 259-69 (1956).
[39]J. A. Fay, "Theory of stagnation point heat transfer in dissociated air," Journal of the Aerospace Sciences **25**(2), 73-85 (1958).
[40]C. S. Kumar, "Experimental investigation of aerodynamic interference heating due to protuberances on flat plates and cones facing hypersonic flows," Ph. D. Dissertation, Dept. of Aerospace Engineering, Indian Institute of Science, Bangalore, November (2013).
[41]D. L. Schultz, and T. V. Jones, "Heat-transfer measurements in short-duration hypersonic facilities," AGARD-AG-165, Paris (France) (1973).
[42]W. J. Cook, and E. J. Felderman, "Reduction of data from thin film heat transfer gauge: A concise numerical technique," AIAA Journal **4**(3), 561-562 (1966).
[43]R. J. Moffat, "Describing the uncertainties in experimental results," Experimental thermal and fluid science, **1**(1), 3-17 (1988).
[44]H. Zhao, and N. Ladommatos, "Optical diagnostics for soot and temperature measurement in diesel engines," Progress in Energy and Combustion Science **24**(3), 221-255 (1998).
[45]F. Payri, J. V. Pastor, J. M. García, and J. M. Pastor, "Contribution to the application of two-color imaging to diesel combustion," Measurement science and technology **18**(8), 2579 (2007).
[46]R. M. Krek, and P. A. Jacobs, "STN, shock tube and nozzle calculations for equilibrium air," Research Report No: 2/93, University of Queensland (1993).
[47]I. M. Vardavas, "Modelling reactive gas flows within shock tunnels," Australian Journal of Physics **37**, 157– 177 (1984).
[48]D. Schuck, "Fiber-based emission spectroscopy on a cylindrical body in the T-ADFA hypersonic shock tunnel," 51st AIAA Aerospace Sciences Meeting including the New Horizons Forum and Aerospace Exposition, 127 (2013).
[49]T. Schott, M. Munk, G. Herring, J. Grinstead, and D. K. Prabhu, "Fiber-based measurement of bow-shock spectra for reentry flight testing," 48th AIAA Aerospace Sciences Meeting including the New Horizons Forum and Aerospace Exposition, 301 (2010).
[50]S. Nomura, H. Takayanagi, K. Fujita, H. Tanno, T. Komuro, and K. Itoh, "Spectroscopic investigation on anomalous heating in free piston shock tunnel HIEST," 11th AIAA/ASME Joint Thermophysics and Heat Transfer Conference, 2545 (2014).
[51]https://www.sharcnet.ca/Software/Fluent6/html/ug/node487.htm
[52]P. G. Huang, J. Bardina, and T. Coakley, "Turbulence modeling validation, testing, and development," NASA Technical Memorandum, 110446, (1997).
[53]http://combustion.berkeley.edu/gri_mech/data/thermo_table.html
[54]http://kinetics.nist.gov/kinetics/KineticsSearchForm.jsp
[55]T. L. Bergman, F. P. Incropera, D. P. DeWitt, and A. S. Lavine, Fundamentals of heat and mass transfer, John Wiley & Sons, (2011).
[56]G. S. Settles, Schlieren and shadowgraph techniques: visualizing phenomena in transparent media, Springer Science & Business Media, (2012).
[57]J. Canny, "A computational approach to edge detection," Readings in Computer Vision, 184-203 (1987).
[58]O. E. Kashireninov, and A. Fontijn, "Modeling of chromium combustion in incineration: Thermochemistry of Cr-CH-Cl combustion in air and selection of key reactions," Combustion and flame **113**(4), 498-506 (1998).
[59]P. A. Gnoffo, "Planetary-entry gas dynamics," Annual Review of Fluid Mechanics **31**(1), 459-494 (1999).

ACCEPTED MANUSCRIPT

ACCEPTED

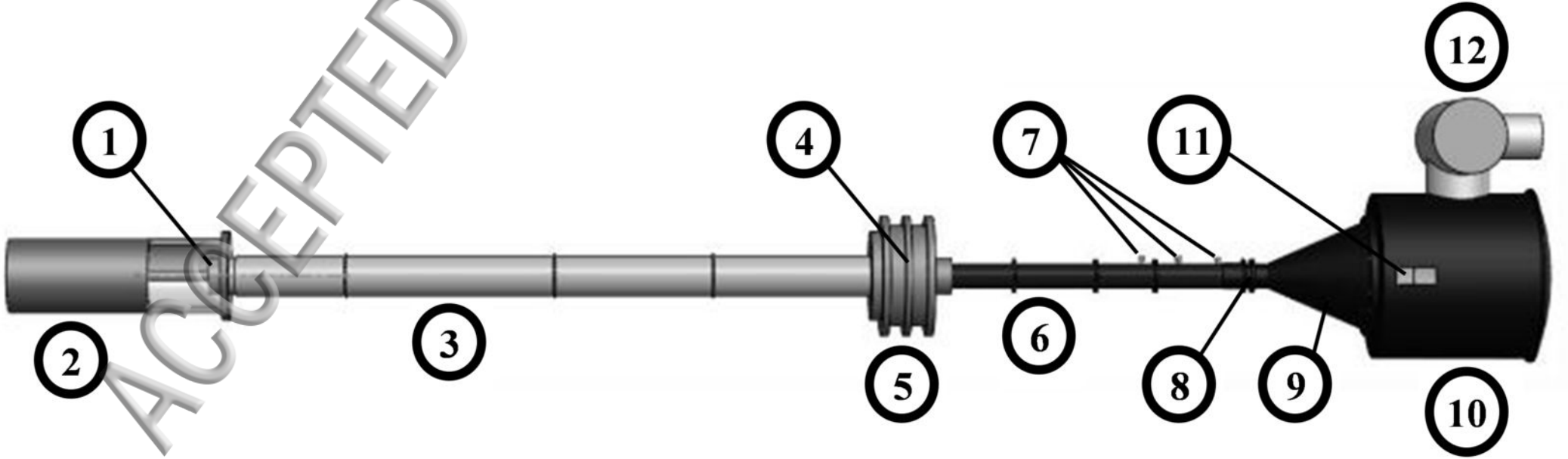

1 Piston
2 Reservoir
3 Compression/ driver tube
4 Location of metal diaphragm
5 Inertial weight
6 Shock/ driven tube
7 Pressure transducers
8 Location of paper diaphragm
9 De Laval (C-D) nozzle
10 Dump tank
11 Optical window
12 High vacuum system

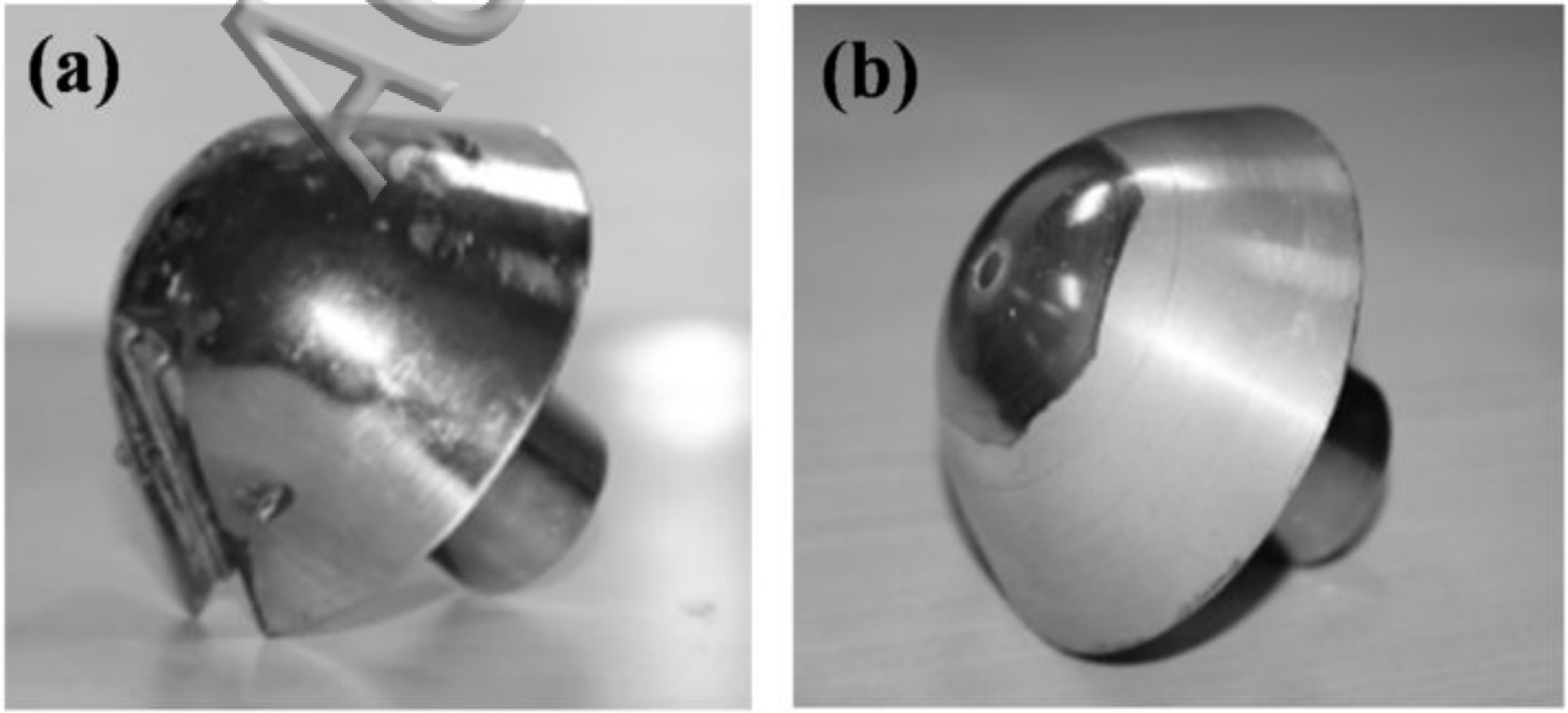
(a)
(b)

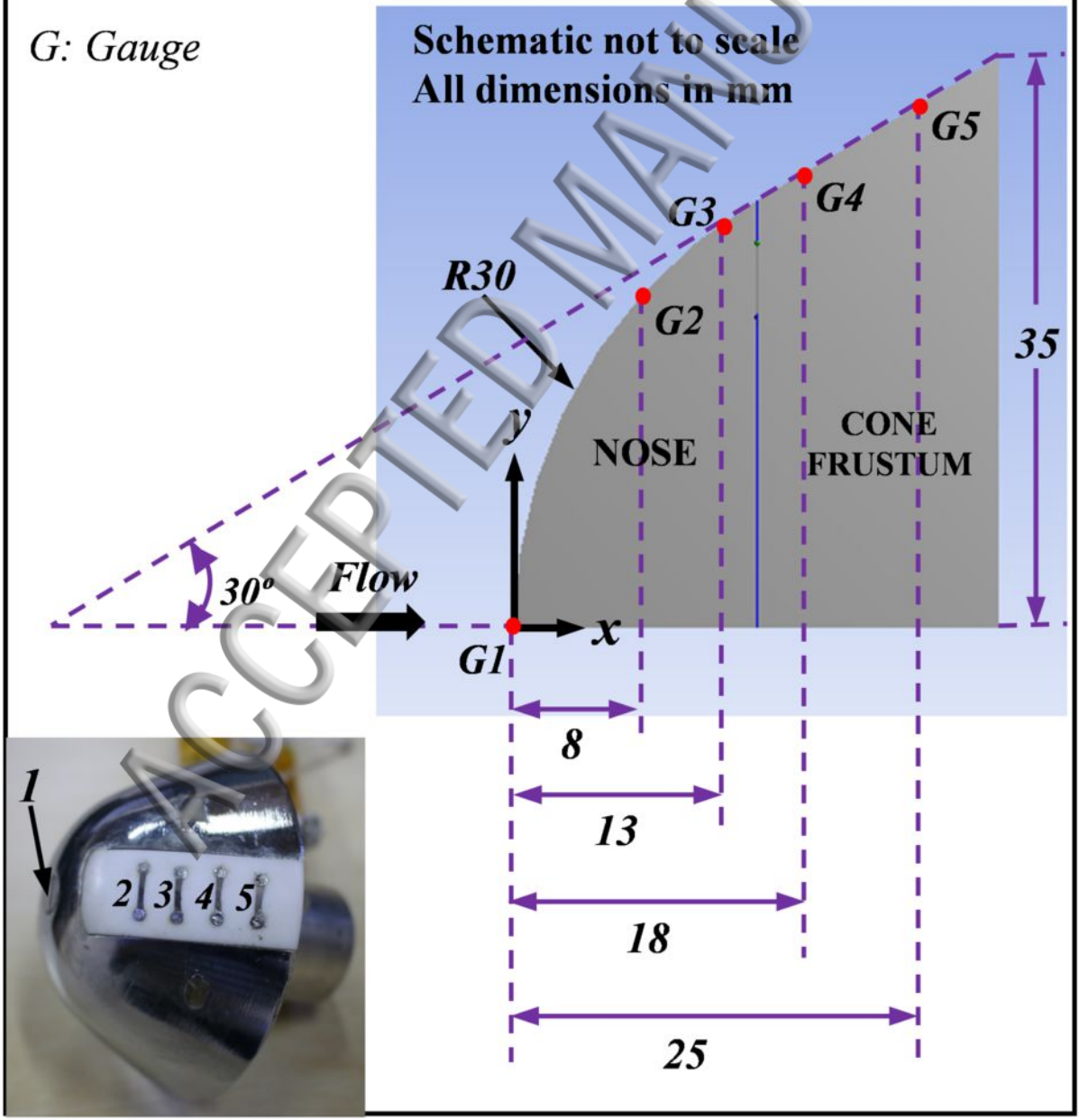

ACCEPTED MANUSCRIPT

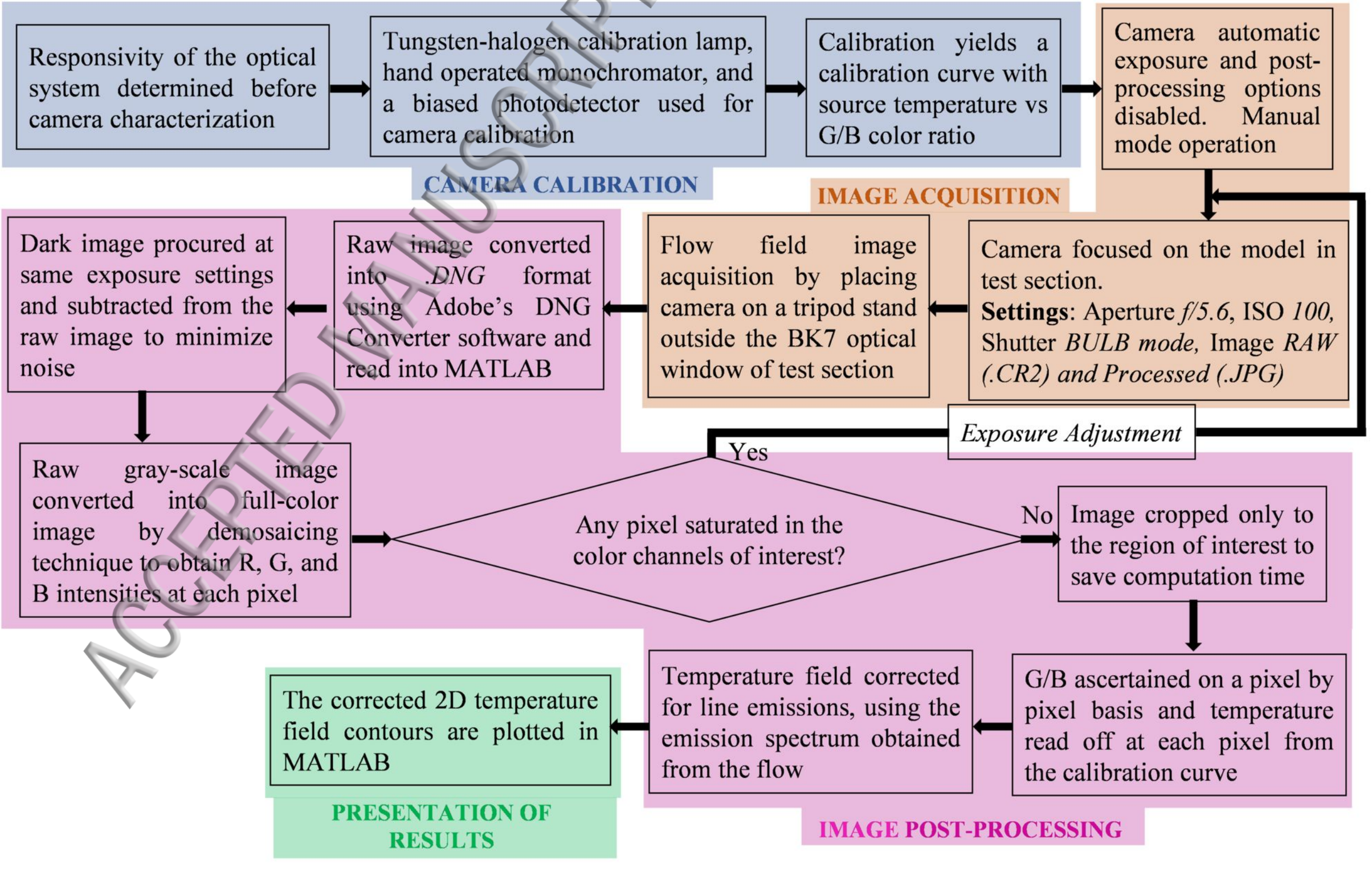

ACCEPTED MANUSCRIPT

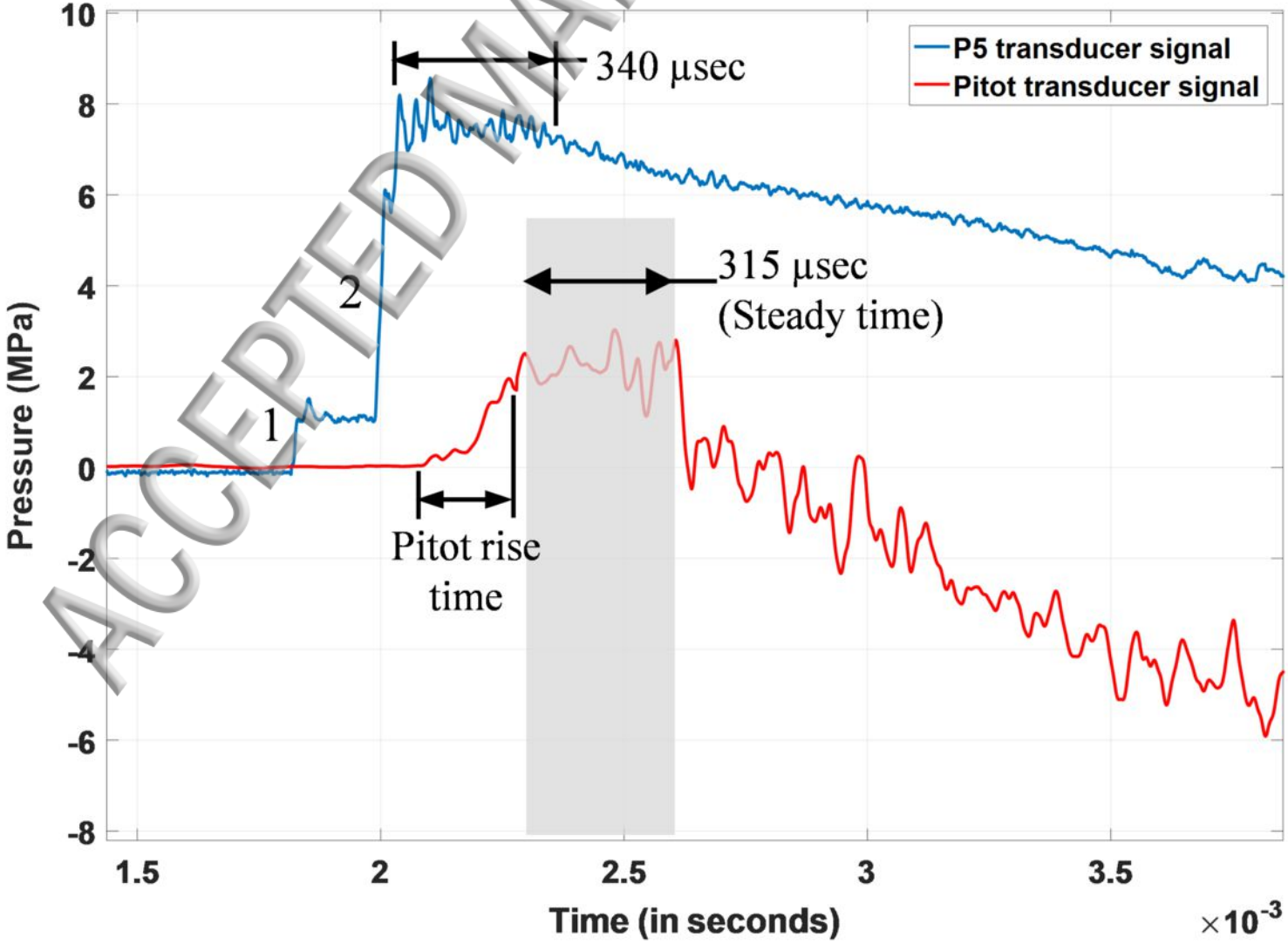

ACCEPTED MANU

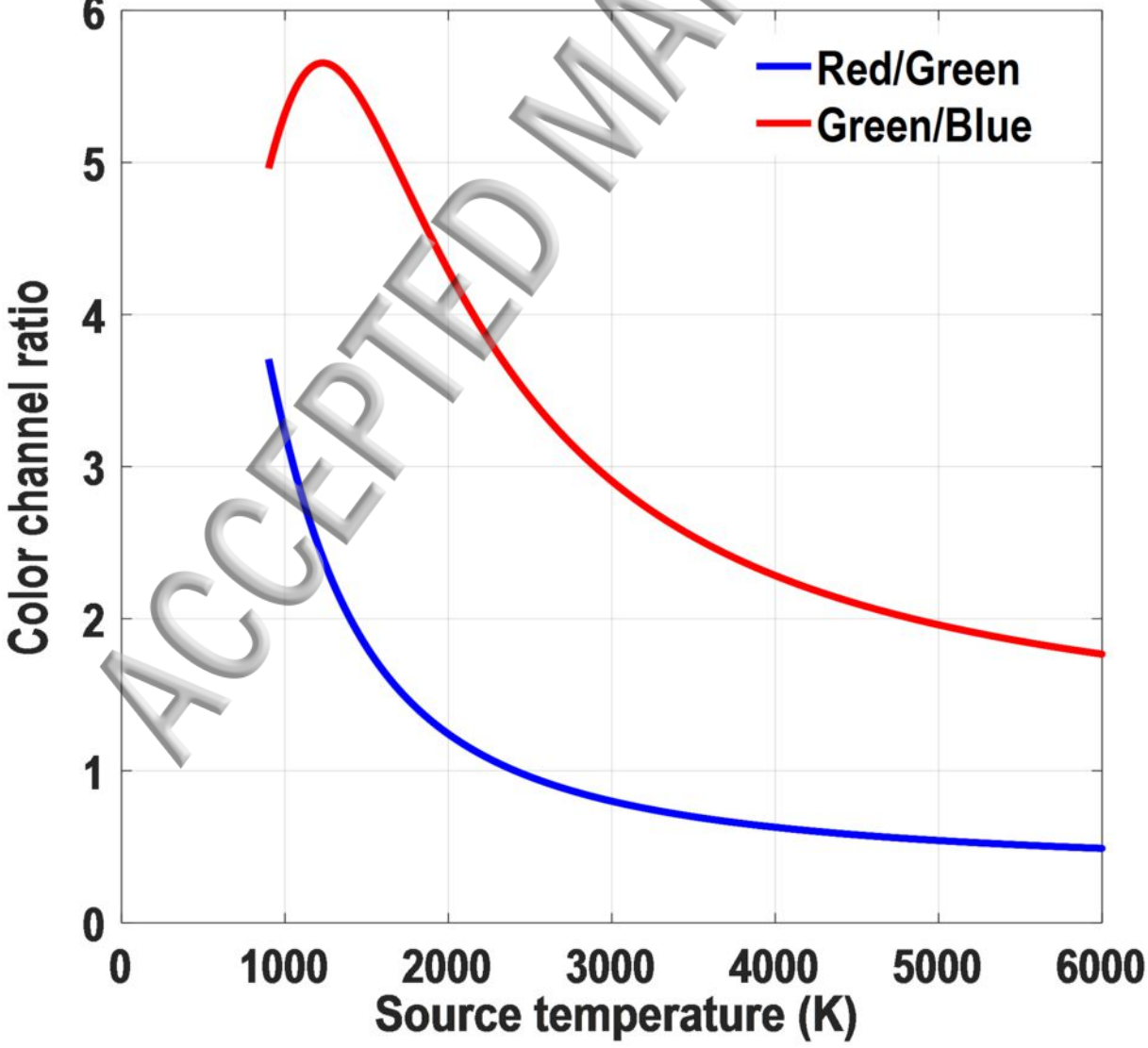

ACCEPTED MANU

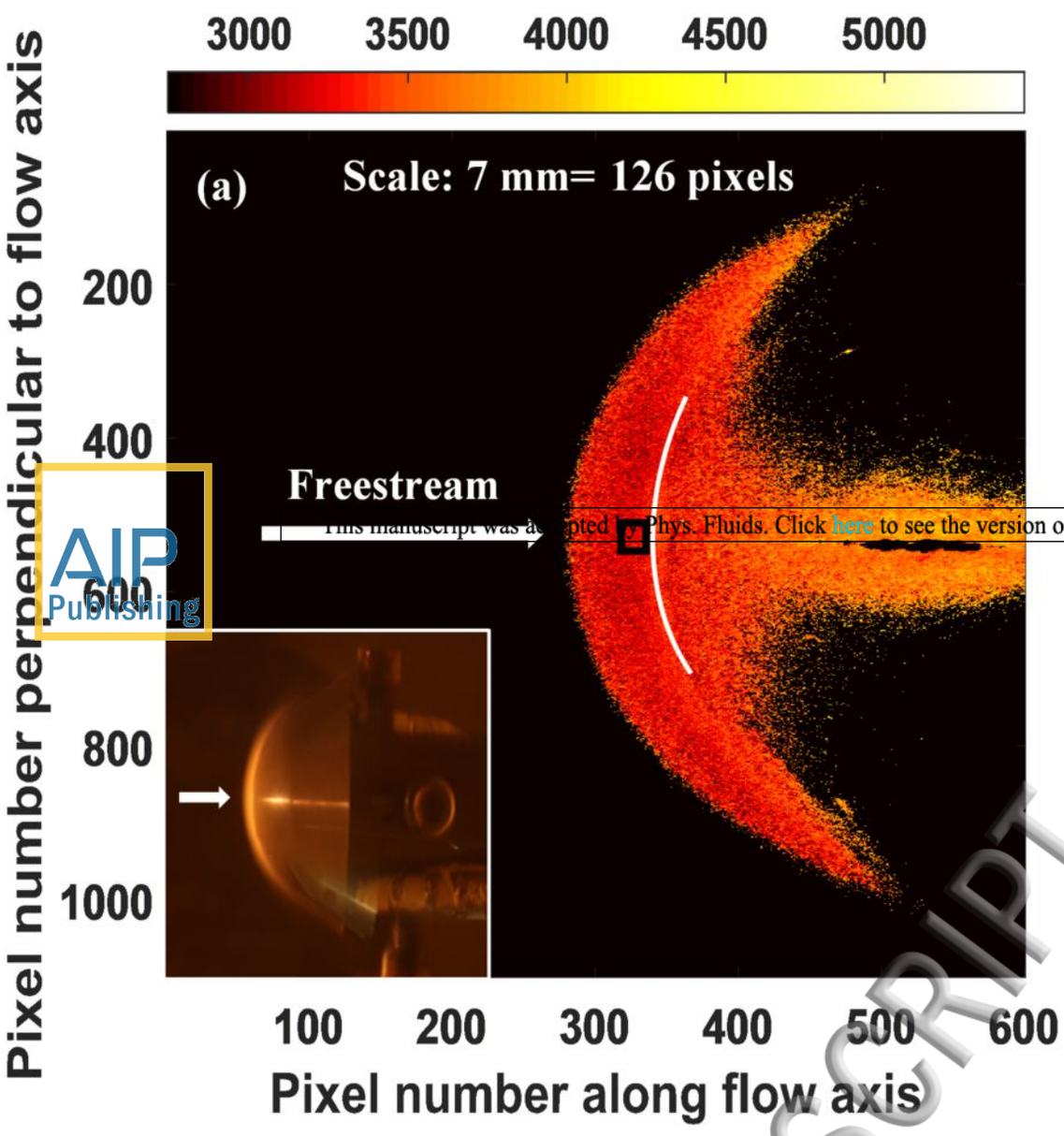

AIP Publishing
This manuscript was accepted by Phys. Fluids. Click here to see the version of record.

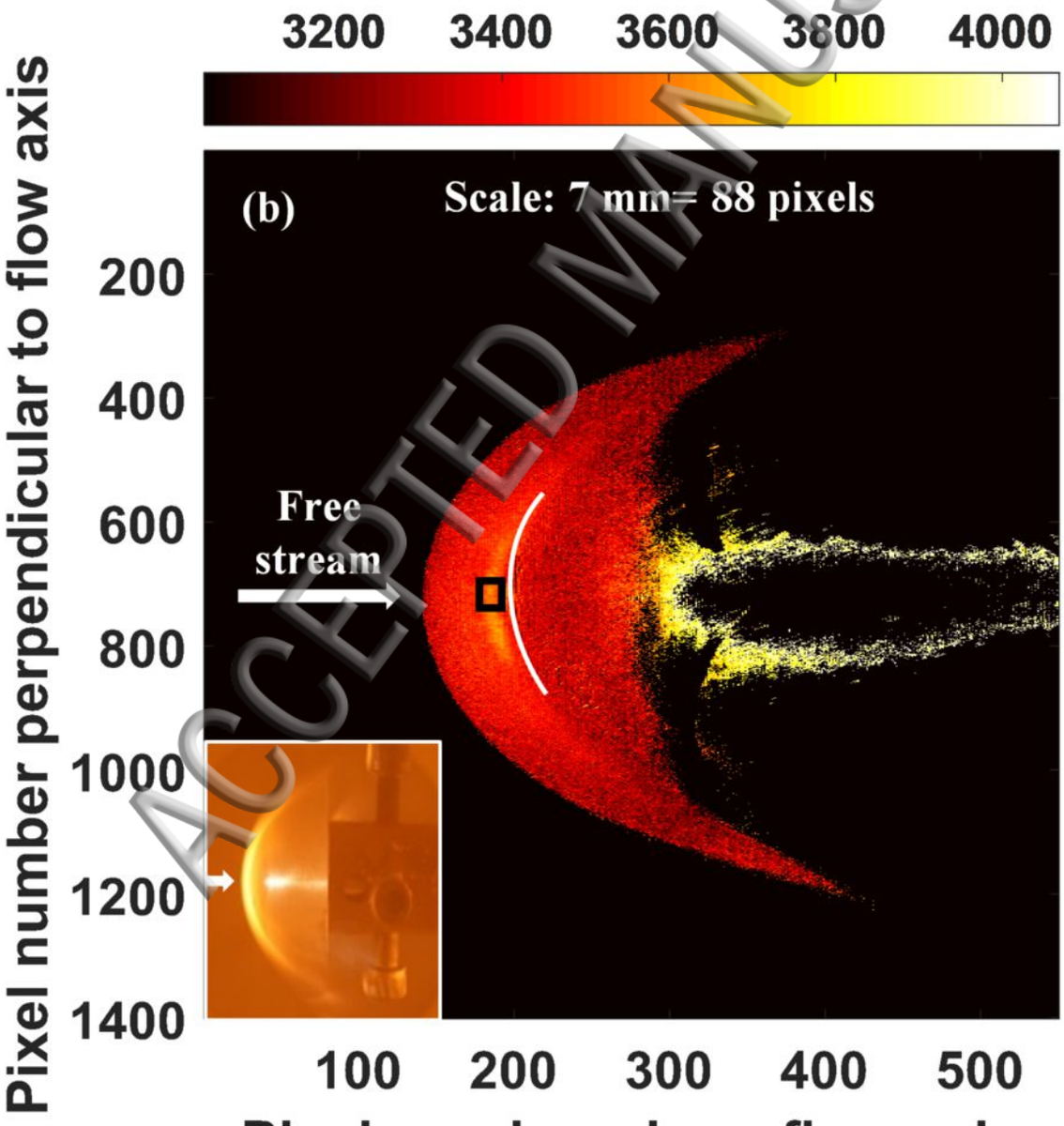

ACCEPTED MANUSCRIPT

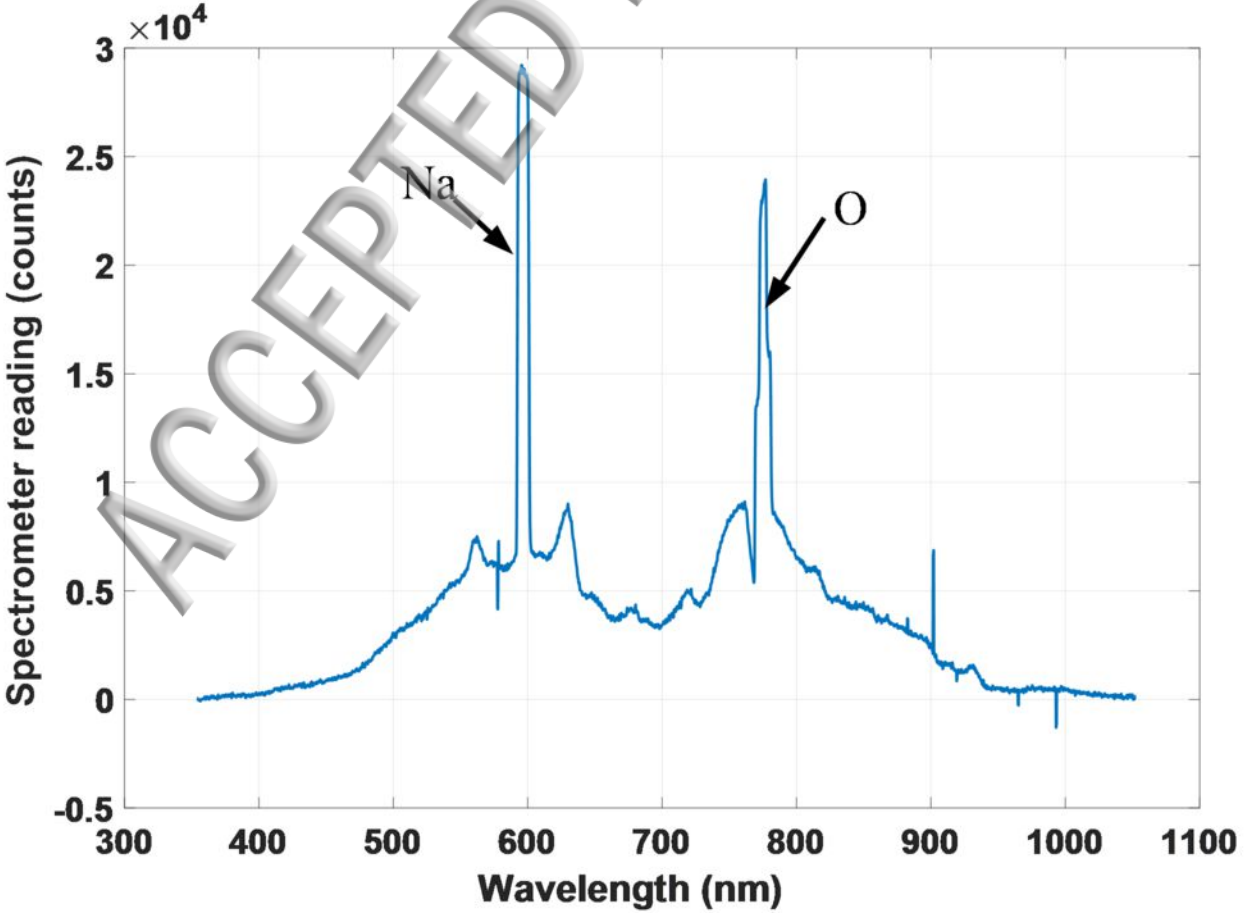
×10^4
3
2.5
2
1.5
1
0.5
0
-0.5
Spectrometer reading (counts)
Na
O
300
400
500
600
700
800
900
1000
1100
Wavelength (nm)
ACCEPTED

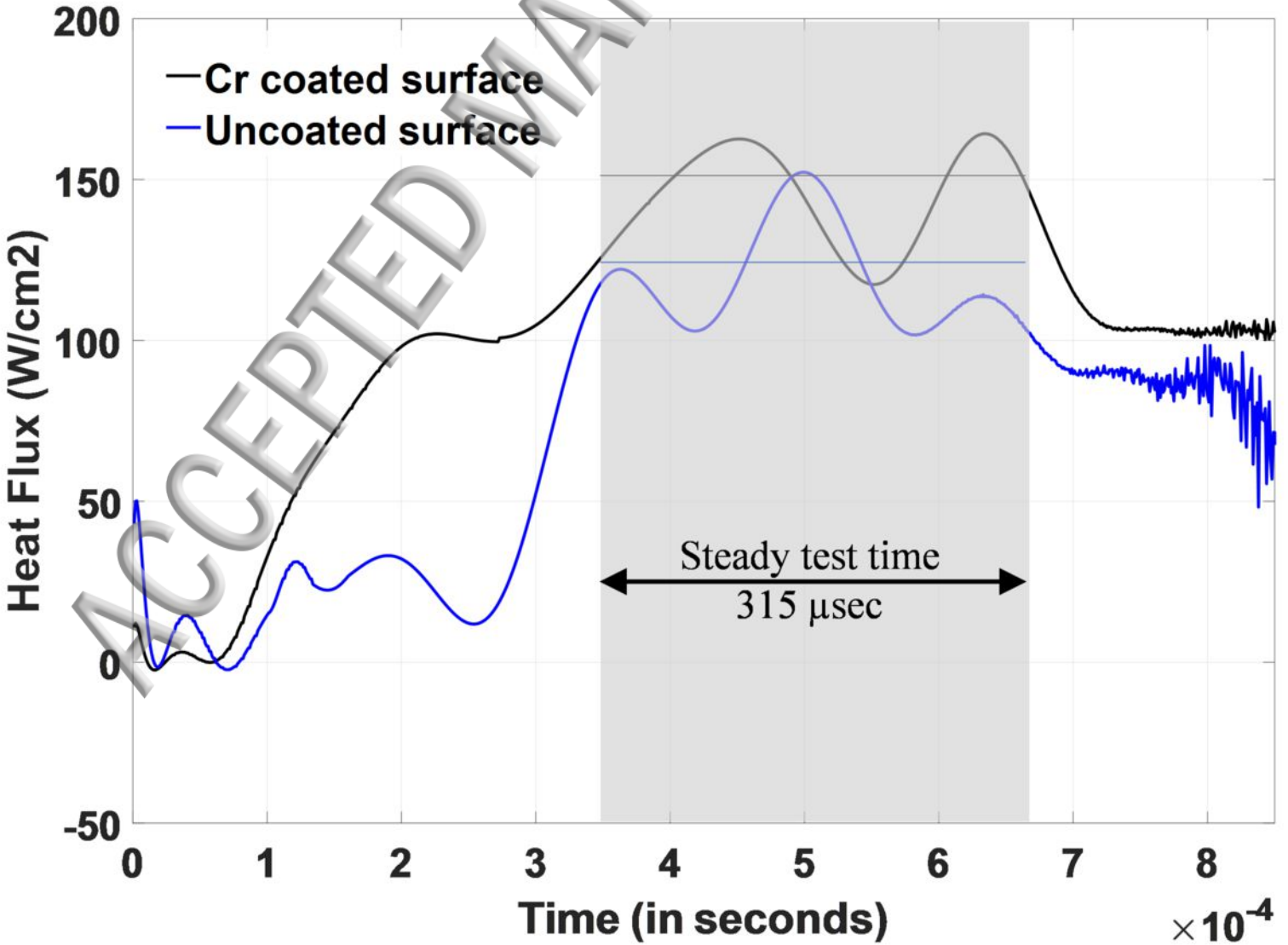

ACCEPTED MANU

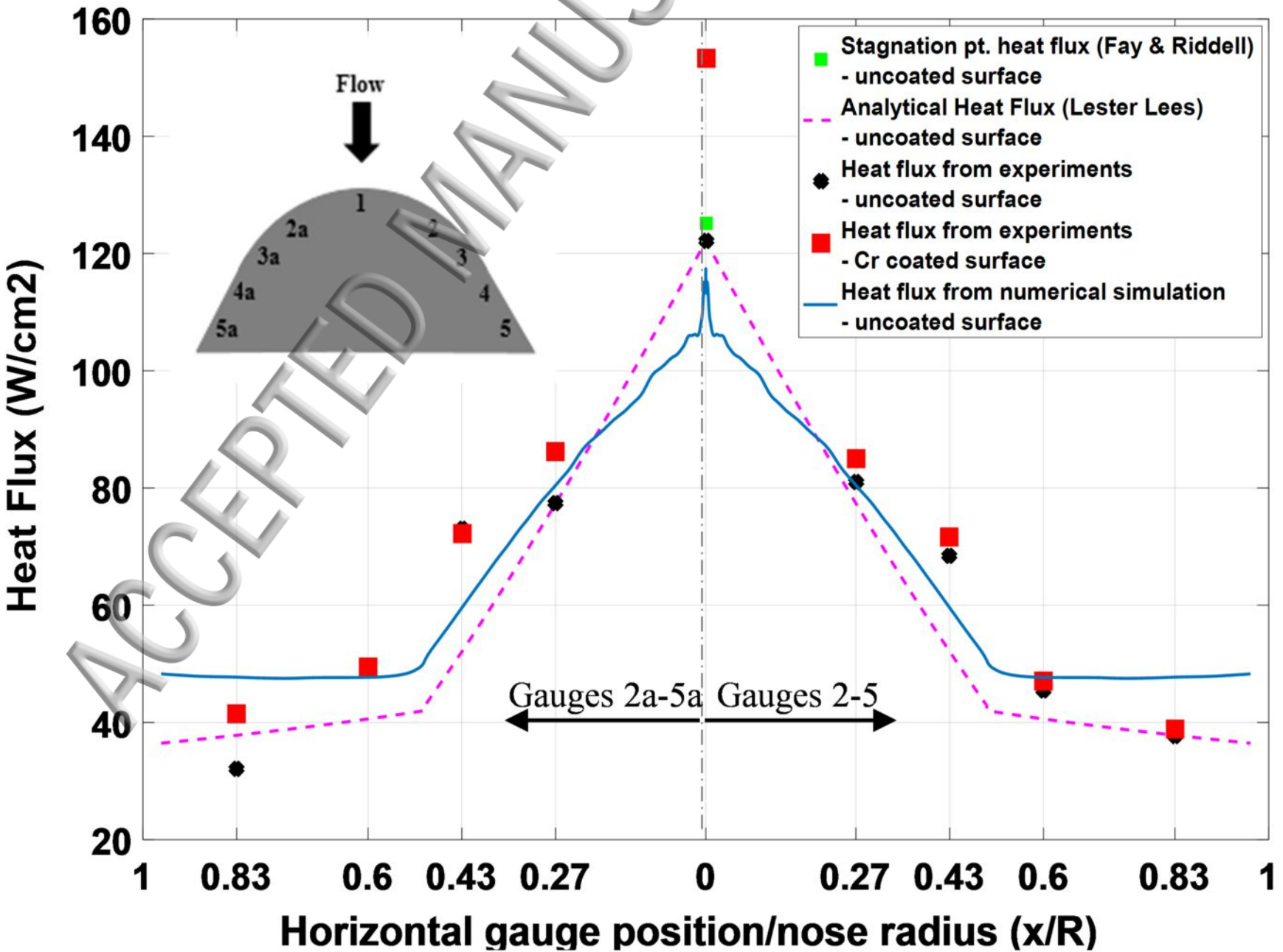

ACCEPTED MANUSCRIPT

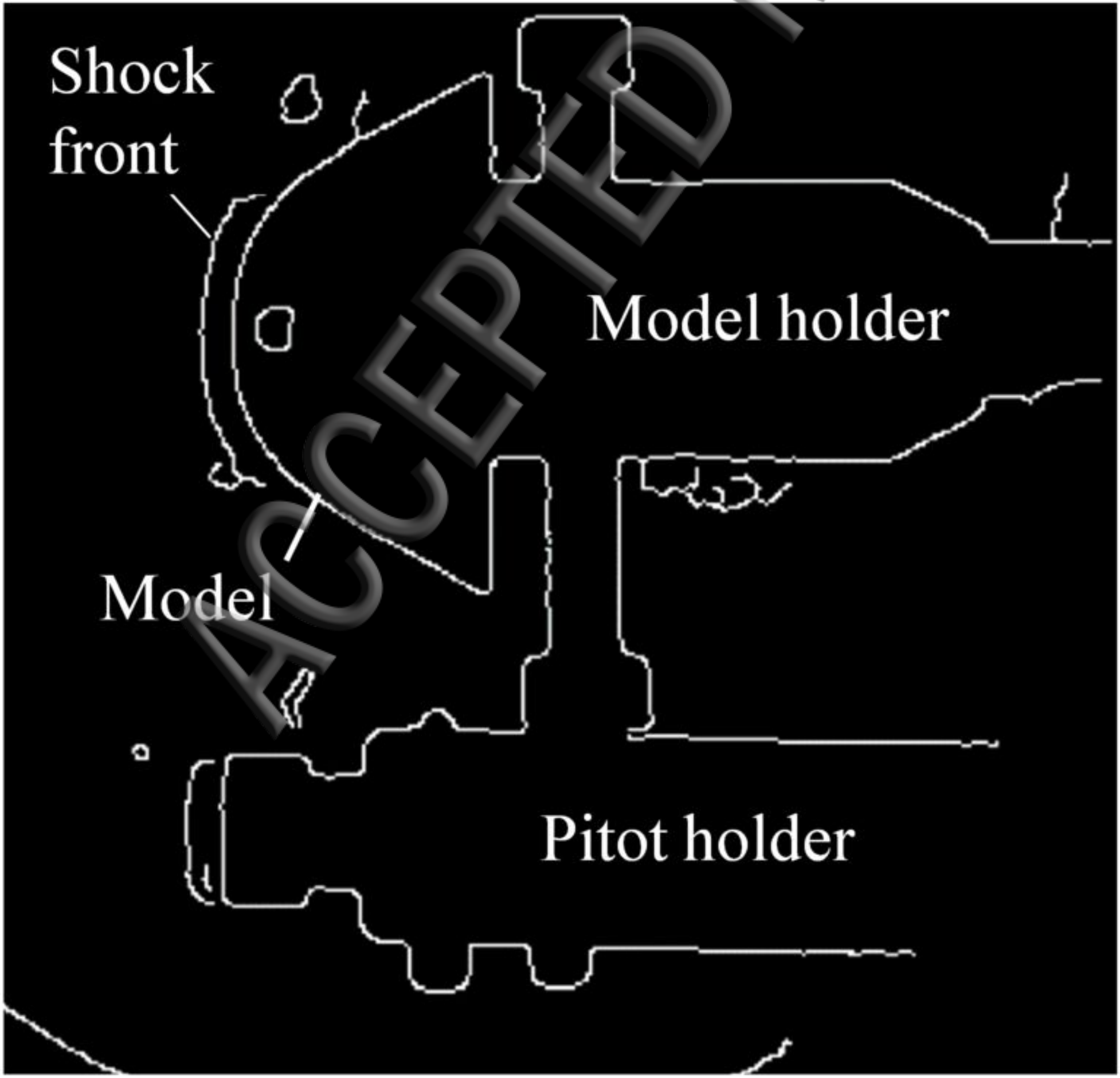
Shock
front
Model holder
Model
Pitot holder

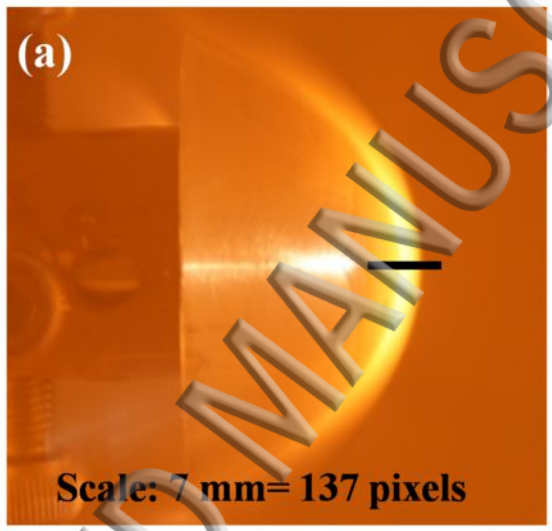

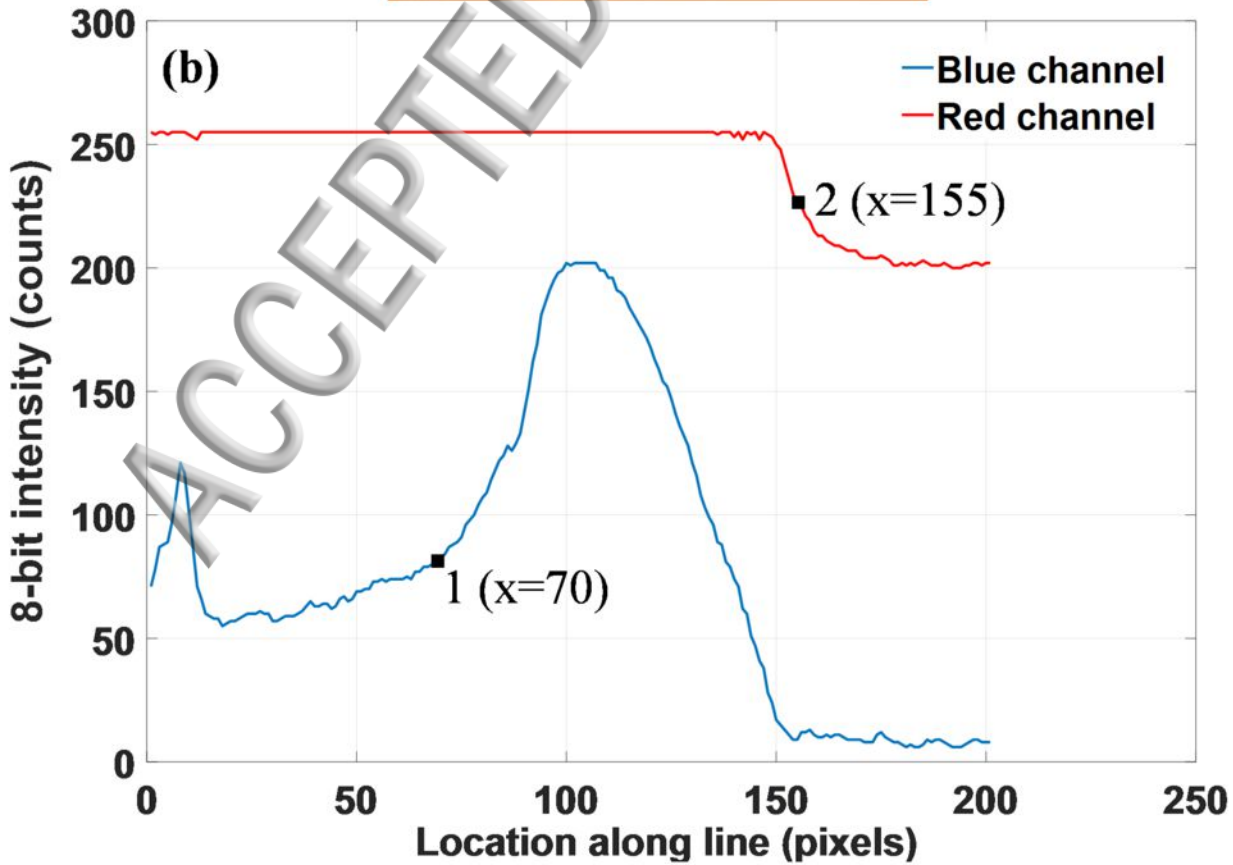

ACCEPTED MANUSCRIPT

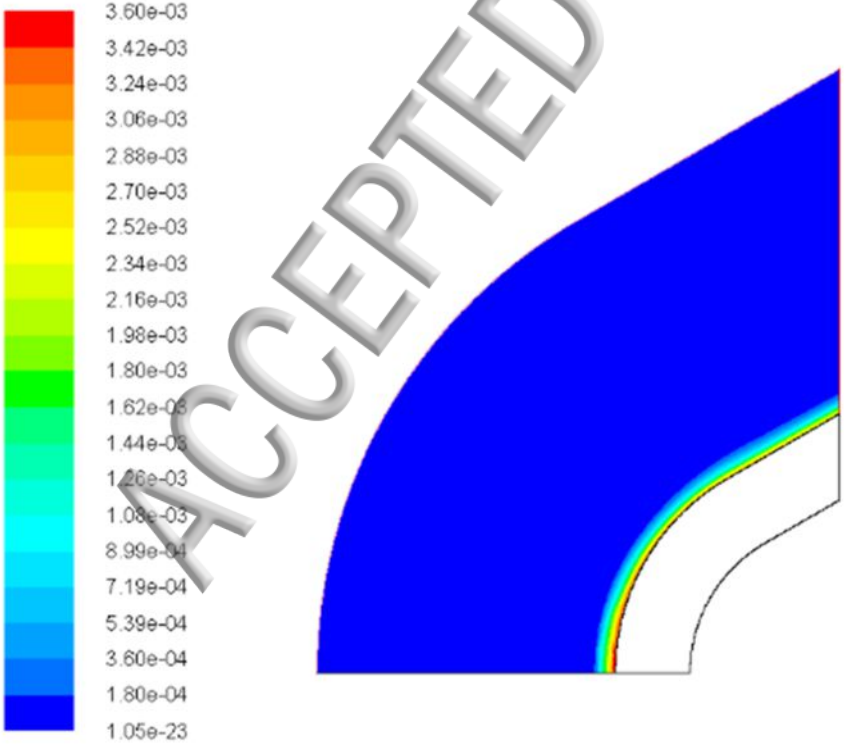

ACCEPTED

ANSYS
R14.5

Contours of Mole fraction of o

Feb 07, 2018
ANSYS Fluent 14.5 (axi, dp, dbns imp, spe, skw)

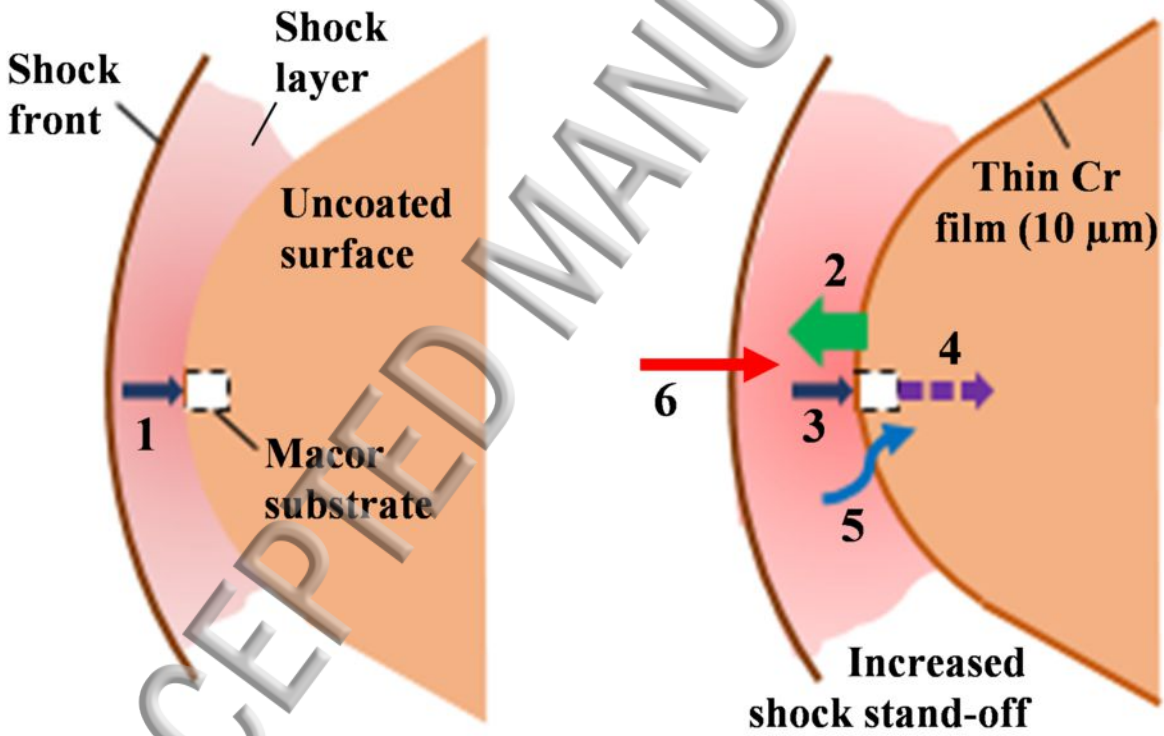

ACCEPTED MANUSCRIPT

1 Convective heat flux at stag. pt. (uncoated)= 122.11 W/cm^2
2 Heat released due to Cr oxidation (H)= 78 W/cm^2
3 Convective total heat flux at stag. pt. with Cr coating= 153.34 W/cm^2
4 Heat loss from Macor rear by conduction= 0.31 W/cm^2
5 Radiative heat flux near stag. pt.= 6.2 W/cm^2
6 Heat used up in raising shock layer temp.= 1.5 W/cm^2
Heat pushing shock layer away from surface (Δh) = 2-(3-1)-4-5-6= 78-(153.34-122.11)-0.31-6.2-1.5 ~ 39 W/cm2

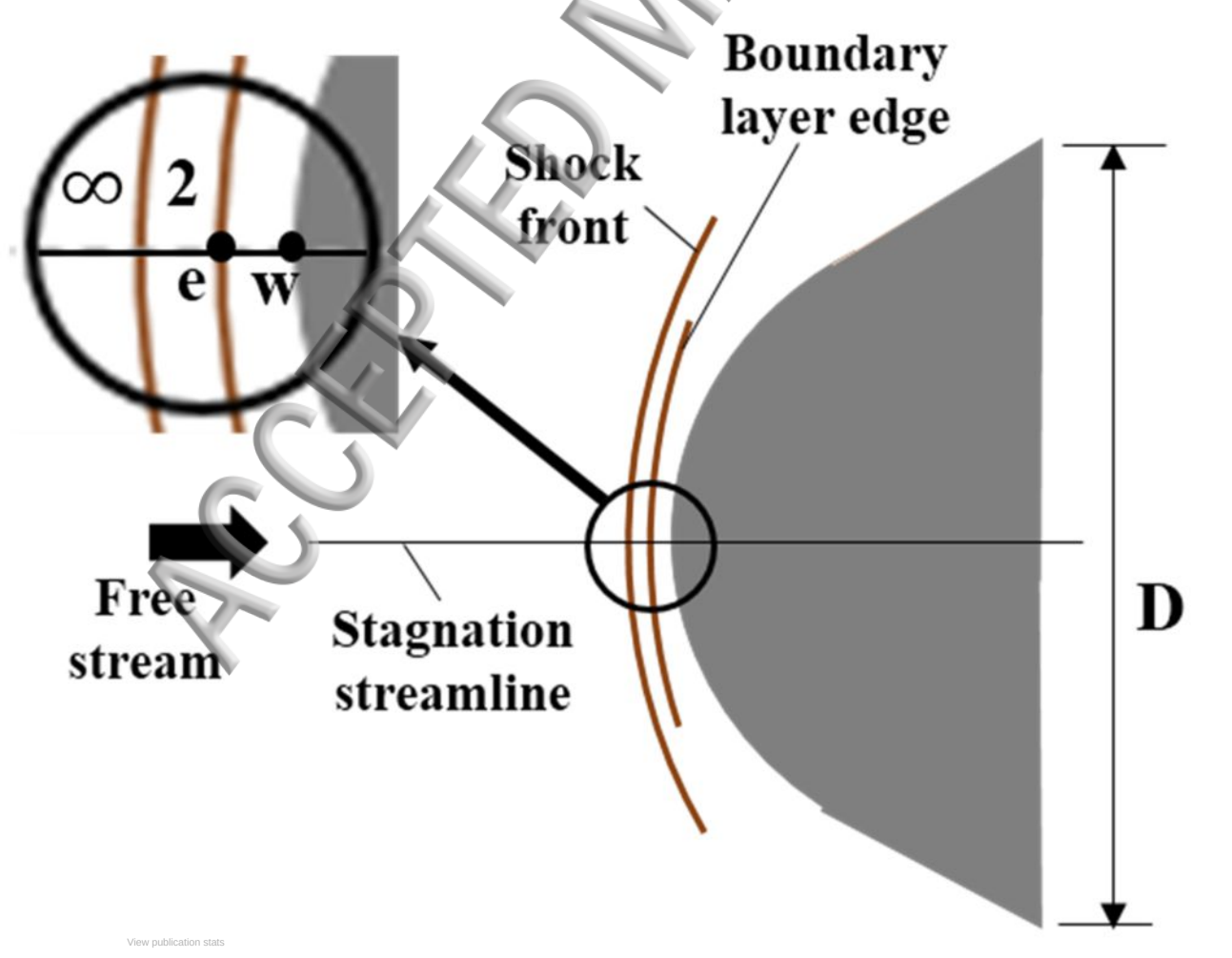

ACCEPTED M

View publication stats